International Journal for Numerical Methods in Engineering

WILEY

RESEARCH ARTICLE

A Total-Lagrangian Material Point Method for Fast and Stable Hydromechanical Modeling of Porous Media

Weijian Liang[1,2] | Bodhinanda Chandra[3] | Jidu Yu[4] | Zhen-Yu Yin[2] | Jidong Zhao[4]

[1]College of Civil and Transportation Engineering, Shenzhen University, Shenzhen, China | [2]Department of Civil and Environmental Engineering, The Hong Kong Polytechnic University, Hung Hom, Hong Kong | [3]Department of Mechanical Engineering, University of California, Berkeley, CA, USA | [4]Department of Civil and Environmental Engineering, Hong Kong University of Science and Technology, Clear Water Bay, Hong Kong

Correspondence: Zhen-Yu Yin (zhenyu.yin@polyu.edu.hk)

Received: 3 July 2025 | **Revised:** 6 September 2025 | **Accepted:** 10 September 2025

Funding: This work was supported by the Research Grants Council (RGC) of Hong Kong (Grant Nos. 15229223, 15232224 and T22-607/24N), and National Science Foundation of China (Grant No. 52508394).

Keywords: fractional step method | incompressible fluid flow | material point method (MPM) | porous media | Total Lagrangian

ABSTRACT

Modeling the incompressible fluid flow in porous media has long been a challenging task in the Material Point Method (MPM). Although widely used, conventional Updated Lagrangian MPM (ULMPM) often suffers from numerical stability and computational efficiency issues in the hydromechanical analysis of saturated porous media. To address these issues, we herein present a novel semi-implicit Total Lagrangian MPM (TLMPM). The proposed TLMPM leverages the fractional step method to decouple pore pressure from kinematic fields and employs the semi-implicit scheme to bypass the small time step constraint imposed by permeability and fluid compressibility. Unlike its UL counterpart, the TLMPM evaluates weighting functions and their gradients only once in the reference configuration, eliminating material point tracking and inherently resolving cell-crossing instabilities. Given the consistent set of active degrees of freedom throughout simulations, the proposed method greatly reduces computational costs associated with system matrix assembly for both kinematics and pore pressure and with free-surface node detection. Furthermore, this feature also facilitates the efficient Cholesky factorization, resulting in a substantial acceleration of the solver performance. The proposed approach has been validated against various benchmark tests, and our results have highlighted the remarkable performance of TLMPM, which can achieve up to 63 times speedup over conventional methods, scaling favorably with problem size, and retaining numerical stability even with low-order basis functions. These advancements position the TLMPM as a transformative tool for poroelastic analysis, with broader applicability to large-deformation problems in geomechanics, energy systems, and environmental engineering.

1 | Introduction

Coupled fluid flow and large deformation behavior in porous media plays a pivotal role in a wide range of geotechnical engineering applications, like landslide [1, 2], hydraulic fracturing [3], and soil-structure interaction [4–7]. Accurate and efficient modeling of the complex interaction between the solid matrix and pore fluid is essential for both a reliable prediction and a robust design of infrastructures. Over the years, a range of numerical strategies has been developed to capture fluid–solid interactions, including classic grid-based finite element methods (FEM) [8–12], entirely Lagrangian particle methods such as smoothed particle hydrodynamics (SPH) [13, 14], and hybrid schemes like the material point method (MPM) [15–17]. Comprehensive reviews of particle methods for FSI can be found in the study [18]. In particular, MPM has emerged as a compelling approach owing to its hybrid Eulerian–Lagrangian description, which combines advantages of mesh-based and meshfree representations for large deformation and contact-dominated FSI problems.

The MPM is featured by its use of material points to carry state variables, and utilizes an Eulerian background mesh to calculate spatial gradients and solve the momentum equation. This hybrid description enables handling problems involving large deformations and evolving interfaces, without suffering from the mesh distortion issues that typically affect the traditional FEM. Early developments in hydromechanical coupled MPM date back to the 2010s [19–25]. These attempts predominantly adopt explicit time integration schemes, where the kinematics of the solid skeleton and pore fluid, as well as their interaction, are computed explicitly.

The explicit scheme is straightforward in implementation and well-suited for transient dynamic problems. However, it is subject to strict time step constraints as it must fulfill the Courant-Friedrichs-Lewy (CFL) condition, which is jointly dictated by the permeability of the porous medium and the bulk modulus of the pore fluid [26]. In practical scenarios, porous media often exhibit low permeability, while pore fluid may be nearly incompressible, leading to prohibitively small time steps. This limitation significantly hinders computational efficiency, particularly in quasi-static problems.

To alleviate these constraints, semi-explicit-implicit integration schemes have been developed [26–30]. By invoking the fractional step method (FSM), the semi-implicit formulation weakly couples the kinematics and the pore pressures, splitting them to be solved sequentially and forming a staggered solution scheme. In particular, the kinematics is resolved explicitly, while the pore pressure is solved implicitly [26]. This formulation permits an equal-order interpolation for both solid and fluid fields, alleviating the time-step restrictions associated with the explicit method. In recent years, the scheme has been further extended to thermo-hydro-mechanical (THM) coupling scenarios [31–35], demonstrating a great potential in large-deformation multiphysics analysis. The semi-implicit MPM generally requires assembling and solving one or a few matrix equations at each step, leading to an increased computational cost. Moreover, spurious pore pressure oscillations may occur due to the cell crossing noise and ill-imposition of Dirichlet and Neumann pressure boundary [36, 37], hence demanding the use of artificial smoothing techniques which may incur substantial diffusive effects.

Despite differences in time integration strategies, both the explicit and semi-implicit MPM formulations build upon an Updated Lagrangian (UL) framework, which continuously tracks the current deformed configuration and uses it to evaluate shape functions and their gradients, as well as to perform numerical integration using particle quadrature. As particles are (always) away from the optimal integration position, this process inevitably leads to quadrature errors [38], especially for low-order interpolation functions with discontinuous shape function gradients [39, 40]. This issue is particularly pronounced when large deformations are present. Recent studies have highlighted the advantages of the Total Lagrangian (TL) MPM, particularly for solid mechanics [41]. Unlike UL-based MPM, TLMPM computes shape functions, their gradient, and kinematics with respect to the initial undeformed configuration (referred to as the reference configuration). This treatment mitigates the drawback associated with continuous updates of the configuration and eliminates the cell-crossing noise that can degrade numerical stability. TLMPM has also been successfully extended to frictional contact problems [42, 43] and combined with FEM in hybrid TLMPM-ULFEM frameworks [44]. However, to the best of the authors' knowledge, its application to multiphysics problems, such as coupled hydromechanical analysis of porous medium, remains unexplored. This work aims to investigate the applicability of TLMPM for this type of problem, highlighting its advantages and limitations, as well as exploring several mitigation measures to alleviate these limitations.

In this study, we present a Total Lagrangian formulation for hydromechanical coupling in saturated porous solids, focusing on its efficient and stable MPM implementation. We concentrate on poroelastic materials undergoing large deformations, such that complications arising from changes in material connectivity due to localized inelastic deformation are initially avoided. The proposed method invokes the fractional step method (FSM) to weakly couple the pore pressure field and the kinematics fields following the UL formulation proposed by [26]. The main difference between the two formulations

is the approach to evaluating shape functions and their gradients, which is performed in the reference configuration, inherently mitigating cell-crossing noise and the associated pore pressure instability issues common in UL-based variants. This strategy ensures that the active degrees of freedom remain unchanged throughout the computation, helping to eliminate the need for particle tracking updates and repeated system matrix assembly for both kinematics and pore pressure solvers. Additionally, the invariance of the coefficient matrix pattern enables the use of numerical factorization, significantly accelerating the linear system solution.

The paper is organized as follows. Section 2 introduces the governing equations for the hydromechanical system. Section 3 presents the TL formulation within the MPM framework, while detailed numerical implementation is described in Section 4. Benchmark and numerical examples that highlight performance comparisons with the ULMPM are provided in Section 5. Finally, conclusions are drawn in Section 7 along with several suggestions for future work.

2 | Formulation and Methodology

2.1 | Prerequisite

In this manuscript, we employ the following notations and conventions. The dot notation $\dot{\square}$ and double dot notation $\ddot{\square}$ denote the first- and second-order material time derivatives, respectively. The symbol $\square \otimes \square$ represents the dyadic (outer) product. Single and double contractions of tensor indices are denoted by $\square \cdot \square$ and $\square : \square$, respectively. Subscripts are used to distinguish different types of variables: The subscript $\square_p$ denotes particle (material point) variables, while $\square_I$ or $\square_J$ represent nodal variables. The subscripts $\square_s$ and $\square_f$ are used to identify quantities associated with the solid skeleton and pore fluid, respectively. $\nabla_x(\square)$ and $\nabla_x \cdot (\square)$ denote the gradient operator and divergence operator with respect to the *current* configuration, respectively, whereas $\nabla_X(\square)$ and $\nabla_X \cdot (\square)$ represent the gradient operator and divergence operator the *reference* configuration, respectively.

2.2 | One-Point Two-Phase MPM and Kinematics

In this study, we adopt the one-point two-phase MPM framework. Each material point represents a mixture of solid skeleton and pore fluid, and their respective volumes V_α ($\alpha = s$ or f) are determined from the corresponding volume fractions θ_α

$$V_\alpha = \theta_\alpha V \tag{1}$$

where V denotes the total mixture volume and we define $\theta_\alpha \equiv \theta_\alpha^t$ as the volume fraction for a specific phase at a given time t. For biphasic (or saturated) porous media, the relationship $\theta_s + \theta_f = 1$ holds. The mass of each phase, m_α, are given by

$$m_\alpha = \theta_\alpha \rho_\alpha V \tag{2}$$

with ρ_α being the intrinsic mass density. Accordingly, the total homogenized mass density for the mixture is

$$\rho = \theta_s \rho_s + \theta_f \rho_f \tag{3}$$

The current configuration of the mixture, Ω, is defined by the deformation mappings of its constituent phases. Specifically, the solid phase is mapped by $\boldsymbol{\varphi}_s(\boldsymbol{X}_s, t)$ and fluid phase by $\boldsymbol{\varphi}_f(\boldsymbol{X}_f, t)$. Here, $\boldsymbol{X}_s \equiv \boldsymbol{X}$ represents the position vector in the reference configuration $\Omega_s^0 \equiv \Omega_0$. The deformation gradient tensor $\boldsymbol{F}$, which relates the current configuration Ω to the reference configuration Ω_0, is defined as:

$$\boldsymbol{F} = \frac{\partial \boldsymbol{x}}{\partial \boldsymbol{X}} \tag{4}$$

where $\boldsymbol{x}$ and $\boldsymbol{X}$ are the current and reference position vectors of the material point, respectively.

In the one-point two-phase MPM formulation, the framework is established such that it can simulate the mechanical deformation of porous materials in the presence of pore fluid. However, the movement of the fluid phase is not fully tracked; specifically, while the equations of motion and mass conservation for the fluid phase are solved locally at each time step, the displacement of fluid particles across time steps is disregarded. It is assumed that the void pore space remains fully saturated at all times. Consequently, as illustrated in Figure 1, the overall deformation of the mixture can be considered to coincide with that of the solid phase, allowing us to equate $\boldsymbol{F} = \boldsymbol{F}_s$.

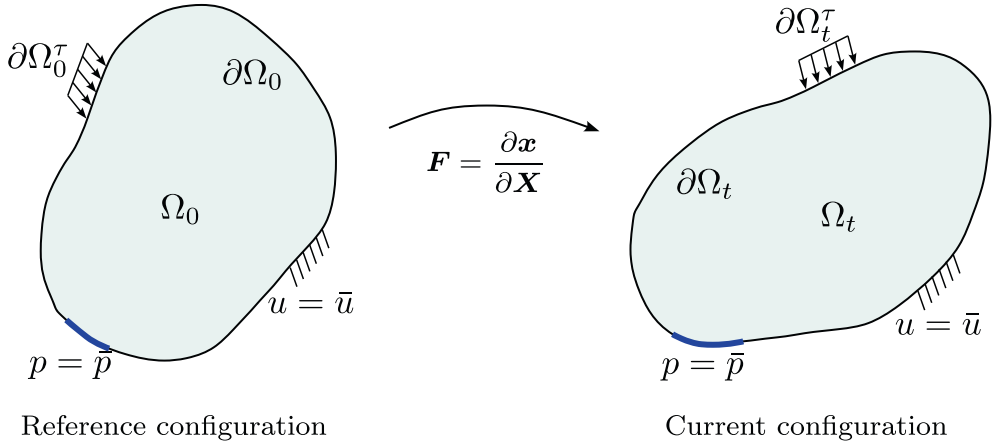

FIGURE 1 | Illustration of the finite deformation in hydromechanical coupling analysis.

The material time derivatives of the position vectors, the velocity, and the acceleration, for each phase can be defined as:

$$\boldsymbol{v}_s = \dot{\boldsymbol{u}}_s = \frac{\mathrm{d}_s \boldsymbol{x}}{\mathrm{d}t}, \qquad \boldsymbol{a}_s = \ddot{\boldsymbol{u}}_s = \frac{\mathrm{d}_s \boldsymbol{v}_s}{\mathrm{d}t} \tag{5}$$

$$\boldsymbol{v}_f = \dot{\boldsymbol{u}}_f, \qquad \boldsymbol{a}_f = \ddot{\boldsymbol{u}}_f = \frac{\mathrm{d}_f \boldsymbol{v}_f}{\mathrm{d}t} = \frac{\mathrm{d}_s \boldsymbol{v}_f}{\mathrm{d}t} + \big((\boldsymbol{v}_f - \boldsymbol{v}_s) \cdot \nabla_x\big)\boldsymbol{v}_f \approx \frac{\mathrm{d}_s \boldsymbol{v}_f}{\mathrm{d}t} \tag{6}$$

Following the same notion of the deformation gradient, the position of the mixture material point is assumed to be governed solely by the solid-phase deformation. Consequently, the Lagrangian time derivative $\mathrm{d}(\cdot)/\mathrm{d}t$ is taken to be equivalent to $\mathrm{d}_s(\cdot)/\mathrm{d}t$, aligning with the solid material point's movement. Advective terms, such as those in Equation (6), are assumed to be small under Darcy's limit (low Reynolds number flow), and thus, often neglected for simplicity. Based on these assumptions, the phase-wise acceleration can be expressed as $\boldsymbol{a}_\alpha = \mathrm{d}_s \boldsymbol{v}_\alpha / \mathrm{d}t$.

2.3 | Compressible Neo–Hookean Model

The compressible Neo–Hookean model is adopted to model the mechanical response of the solid skeleton [45]. The strain energy density function ψ of the material is expressed as:

$$\psi = \frac{\mu}{2}\big(I_1 - d\big) - \mu \ln J + \frac{\lambda}{2}(\ln J)^2 \tag{7}$$

where λ and μ are the first and second Lamé parameters of the solid skeleton, respectively. Here, $I_1 = \mathrm{tr}(\boldsymbol{C})$ represents the first invariant of the right Cauchy–Green deformation tensor $\boldsymbol{C} = \boldsymbol{F}^\top \boldsymbol{F}$, and $J = \det(\boldsymbol{F})$ denotes the Jacobian. The parameter d denotes the spatial dimension, which is set to 2 in this study.

Differentiating the strain energy density function ψ with respect to the deformation, the effective Cauchy stress tensor for the solid phase is derived as:

$$\boldsymbol{\sigma}' = \frac{\mu}{J}\big(\boldsymbol{F}\boldsymbol{F}^T - \boldsymbol{I}\big) + \frac{\lambda \ln J}{J}\,\boldsymbol{I} \tag{8}$$

where $\boldsymbol{I}$ is the second-order identity tensor.

Following Terzaghi's effective stress principle [46], the total Cauchy stress tensor $\boldsymbol{\sigma}$ can be decomposed into solid-phase and pore-fluid phase components as:

$$\boldsymbol{\sigma} = \boldsymbol{\sigma}' - p\boldsymbol{I} \tag{9}$$

where p denotes the pore pressure. In the notation adopted herein, stress is considered positive in tension, whereas pore fluid pressure is positive in compression.

For the Total Lagrangian formulation, it is convenient to work with the first Piola–Kirchhoff stress $\boldsymbol{P}$, which is associated with the Cauchy stress tensor $\boldsymbol{\sigma}$ via:

$$\boldsymbol{\sigma} = \frac{1}{J}\boldsymbol{P}\boldsymbol{F}^T \tag{10}$$

By performing a similar stress pull-back to Equation (9), the total first Piola-Kirchhoff stress is obtained as:

$$\boldsymbol{P} = \boldsymbol{P}' - pJ\boldsymbol{F}^{-T} \tag{11}$$

where $\boldsymbol{P}' = J\boldsymbol{\sigma}'\boldsymbol{F}^{-T}$ is the effective first Piola–Kirchhoff stress and $pJ\boldsymbol{F}^{-T}$ represents the contribution from the pore pressure.

2.4 | Mass Conservation

Assuming no mass exchange occurs between the solid and fluid phases, the mass balance equations for each phase can be expressed as [26]:

$$\frac{\mathrm{d}_\alpha m_\alpha}{\mathrm{d}t} = \frac{\mathrm{d}_\alpha}{\mathrm{d}t}(\theta_\alpha \rho_\alpha) + \theta_\alpha \rho_\alpha \nabla_x \cdot \boldsymbol{v}_\alpha = 0 \tag{12}$$

In this study, both solid grains and interstitial pore fluid are assumed to be fully incompressible ($\mathrm{d}\rho_\alpha/\mathrm{d}t = 0$), and hence the mass balance equation simplifies to the following form:

$$\frac{\mathrm{d}_\alpha \theta_\alpha}{\mathrm{d}t} + \theta_\alpha \nabla_x \cdot \boldsymbol{v}_\alpha = 0 \tag{13}$$

By summing the mass balance equations for both phases and noting that the total volume fraction sums to unity ($\theta_s + \theta_f = 1$ for a saturated porous medium), the mass conservation equation for the mixture is derived as:

$$\nabla_x \cdot \left(\theta_s \boldsymbol{v}_s + \theta_f \boldsymbol{v}_f\right) = 0 \tag{14}$$

In the one-point two-phase MPM implementation, it is common to assume that the spatial variation of the phase-wise volume fraction is negligible across the mixture [26], and therefore Equation (14) can be simplified to:

$$\theta_s \nabla_x \cdot \boldsymbol{v}_s + \theta_f \nabla_x \cdot \boldsymbol{v}_f = 0 \tag{15}$$

Considering the deformation of the material point is assumed to follow the solid phase, we can relate the current volume fraction to its initial value via the Jacobian $J = J_s = \det \boldsymbol{F}_s$:

$$\theta_s = \theta_s^0/J, \qquad \theta_f = 1 - (1 - \theta_f^0)/J \tag{16}$$

2.5 | Momentum Conservation

Neglecting convective terms, the linear momentum balance equations for the solid skeleton and the pore fluid are given by:

$$\theta_s \rho_s \boldsymbol{a}_s = \nabla_x \cdot \left(\boldsymbol{\sigma}' - \theta_s p \boldsymbol{I}\right) + \theta_s \rho_s \boldsymbol{b} - \boldsymbol{f}_d - \boldsymbol{f}_b \tag{17}$$

$$\theta_f \rho_f \boldsymbol{a}_f = -\nabla_x\left(\theta_f p\right) + \theta_f \rho_f \boldsymbol{b} + \boldsymbol{f}_d + \boldsymbol{f}_b \tag{18}$$

where $\boldsymbol{b}$ is the body force per unit mass (e.g., gravitational acceleration). In the above expressions, the viscous drag and buoyant force in the current configuration are denoted as $\boldsymbol{f}_d$ and $\boldsymbol{f}_b$, respectively. They are given by:

$$\boldsymbol{f}_d = -\frac{\theta_f^2 \rho_f g}{k}\left(\boldsymbol{v}_f - \boldsymbol{v}_s\right) \tag{19}$$

$$\boldsymbol{f}_b = p \nabla_x \theta_f \tag{20}$$

Here, the drag force is considered to follow the linear Darcy's law, where $g = 9.81$ m/s is the gravitational acceleration and k is the soil permeability (hydraulic conductivity).

2.6 | Semi-Explicit-Implicit Integration and Fractional Step Method

Although explicit schemes are straightforward to implement, they are often unsuitable for fully or weakly incompressible materials, such as porous media saturated with pore water. This limitation arises from the requirement of significantly small time steps to ensure stability. In this study, we adopt the semi-explicit-implicit scheme [26] for temporal discretization, which will be briefly summarized in this section. In this approach, the effective stress is solved explicitly to circumvent the computational cost and complexity of formulating the consistent tangent operator for nonlinear elastoplastic materials. Meanwhile, the pore pressure is solved implicitly to overcome the time step restriction. Noted that, in this study, we focus exclusively on highly deformable poroelastic materials. The implementation and extension of the method to include poroelastoplastic materials are reserved for future work.

The fractional step method (FSM), also referred to as the splitting method, separates the computation of pore pressure from other kinematic variables. By introducing intermediate velocities ($\boldsymbol{v}_\alpha^*,\ \alpha = s, f$), the coupled system is advanced to the next step through multiple substeps, with each substep addressing a single variable independently. The procedure is outlined as follows:

$$\{\boldsymbol{v}_\alpha^t, p^t\} \xrightarrow{\text{prediction}} \{\boldsymbol{v}_\alpha^*\} \xrightarrow{\text{pressure solution}} \{p^{t+1}\} \xrightarrow{\text{correction}} \{\boldsymbol{v}_\alpha^{t+1}\} \tag{21}$$

In the FSM, first, the inertial terms are decomposed into predictor and corrector, and related to $\boldsymbol{v}_\alpha^*$ as below:

$$\boldsymbol{a}_\alpha^t = \frac{\boldsymbol{v}_\alpha^{t+1} - \boldsymbol{v}_\alpha^t}{\Delta t} = \underbrace{\frac{\boldsymbol{v}_\alpha^* - \boldsymbol{v}_\alpha^t}{\Delta t}}_{\boldsymbol{a}_\alpha^*} + \underbrace{\frac{\boldsymbol{v}_\alpha^{t+1} - \boldsymbol{v}_\alpha^*}{\Delta t}}_{\boldsymbol{a}_\alpha^{**}} \tag{22}$$

With the predicted kinematic variables, the momentum balance equations are split to isolate the pore pressure p^{t+1} from the acceleration $\boldsymbol{a}_\alpha^{t+1}$. They are presented as:

Solid phase:

$$\theta_s \rho_s \boldsymbol{a}_s^* = \nabla_x \cdot \boldsymbol{\sigma}'^{,t} - \theta_s \nabla_x p^t + \theta_s \rho_s \boldsymbol{b} + \frac{\theta_f^2 \rho_f g}{k}(\boldsymbol{v}_f^* - \boldsymbol{v}_s^*) \tag{23}$$

$$\theta_s \rho_s \boldsymbol{a}_s^{**} = -\theta_s \nabla_x \left(p^{t+1} - p^t\right) \tag{24}$$

Fluid phase:

$$\theta_f \rho_f \boldsymbol{a}_f^* = -\theta_f \nabla_x p^t + \theta_f \rho_f \boldsymbol{b} - \frac{\theta_f^2 \rho_f g}{k}(\boldsymbol{v}_f^* - \boldsymbol{v}_s^*) \tag{25}$$

$$\theta_f \rho_f \boldsymbol{a}_f^{**} = -\theta_f \nabla_x \left(p^{t+1} - p^t\right) \tag{26}$$

Mixture:

$$\theta_s \rho_s \boldsymbol{a}_s^* + \theta_f \rho_f \boldsymbol{a}_f^* = \nabla_x \cdot (\boldsymbol{\sigma}'^{,t} - p^t) + \rho \boldsymbol{b} \tag{27}$$

$$\theta_s \rho_s \boldsymbol{a}_s^{**} + \theta_f \rho_f \boldsymbol{a}_f^{**} = -\nabla_x \left(p^{t+1} - p^t\right) \tag{28}$$

It is also worth noting that alternative methods for treating drag force Equations (23) and (25) are available [47, 48]. Herein, we follow our previous work [26] and evaluate this term implicitly based on the predicted velocities, which reads:

$$\boldsymbol{f}_d = -\frac{\theta_f^2 \rho_f g}{k}(\boldsymbol{v}_f^* - \boldsymbol{v}_s^*) = -\frac{\theta_f^2 \rho_f g}{k}\left((\boldsymbol{v}_f^t - \boldsymbol{v}_s^t) + \Delta t(\boldsymbol{a}_f^* - \boldsymbol{a}_s^*)\right) \tag{29}$$

Upon computing the predicted accelerations via Equations (23) and (25), the intermediate velocities $\boldsymbol{v}_\alpha^*$ can be subsequently calculated. These intermediate velocities are then substituted into the continuity equation (Equation (15)), which further yields the Poisson equation for the incremental pore pressure, $\Delta p^{t+1} = p^{t+1} - p^t$, that is,

$$\Delta t\left(\frac{\theta_s}{\rho_s} + \frac{\theta_f}{\rho_f}\right)\nabla_x^2\left(\Delta p^{t+1}\right) = \theta_s \nabla_x \cdot \boldsymbol{v}_s^* + \theta_f \nabla_x \cdot \boldsymbol{v}_f^* \tag{30}$$

After solving the Poisson equation to obtain the updated pore water pressure p^{t+1}, Equations (24) and (26) are utilized to compute the updated velocities $\boldsymbol{v}_\alpha^{t+1}$, completing the computation process in a single time step.

Remark 1. It is worth emphasizing that, although various formulations can be adopted, our implementation of the FSM-based MPM employs the momentum equations for the mixture and fluid phases to predict the intermediate acceleration and velocity. This option is chosen as it can simplify the enforcement of total external forces on the mixture and pore water components, which can be seamlessly aligned with typical experimental measurements.

Remark 2. In the current study, we employed the incremental form of the FSM-MPM, which is demonstrated by [26] to perform better in poromechanics simulations. Another alternative form, which solves the total pore pressure, p^{t+1}, implicitly via a Poisson equation, has also been proposed in the literature. Interested readers are referred to [26, 49] for further details.

2.7 | Weak Form

Following the Bubnov–Galerkin method, the weak form of the momentum equation at the prediction stage in the current configuration Ω_t is derived as follows:

$$\begin{aligned}\int_{\Omega_t} \delta\boldsymbol{v}\cdot\left(\theta_s\rho_s\boldsymbol{a}_s^*\right)d\Omega_t+\int_{\Omega_t}\delta\boldsymbol{v}\cdot\left(\theta_f\rho_f\boldsymbol{a}_f^*\right)d\Omega_t=-\int_{\Omega_t}\nabla_x\delta\boldsymbol{v}:\left(\boldsymbol{\sigma}'^{,t}-p^t\boldsymbol{I}\right)d\Omega_t\\+\int_{\Omega_t}\delta\boldsymbol{v}\cdot\rho\boldsymbol{b}d\Omega_t+\int_{\partial\Omega_t^\tau}\delta\boldsymbol{v}\cdot\boldsymbol{\tau}dS_t\end{aligned}\tag{31}$$

$$\begin{aligned}\int_{\Omega_t}\delta\boldsymbol{v}\cdot\left(\theta_f\rho_f\boldsymbol{a}_f^*\right)d\Omega_t=\int_{\Omega_t}\left(\nabla_x\cdot\delta\boldsymbol{v}\right)\theta_f p^t d\Omega_t-\int_{\Omega_t}\delta\boldsymbol{v}\cdot\left(\frac{\theta_f^2\rho_f g}{k}\left(\boldsymbol{v}_f^*-\boldsymbol{v}_s^*\right)\right)d\Omega_t\\+\int_{\Omega_t}\delta\boldsymbol{v}\cdot\theta_f\rho_f\boldsymbol{b}d\Omega_t+\int_{\partial\Omega_t^p}\delta\boldsymbol{v}\cdot\bar{\boldsymbol{t}}_f dS_t\end{aligned}\tag{32}$$

Here, $\delta\boldsymbol{v}$ denotes the test function, with $\delta\boldsymbol{v}=\boldsymbol{0}$ on boundaries where solid or fluid displacements (or velocities) are prescribed. Meanwhile, $\boldsymbol{\tau}=\boldsymbol{\sigma}\cdot\boldsymbol{n}$ is the surface traction that acts on the boundary $\partial\Omega_t^\tau$ of the mixture, with $\boldsymbol{n}$ being the unit outward normal to the boundary, and $\bar{\boldsymbol{t}}_f=-\theta_f p\boldsymbol{I}\cdot\boldsymbol{n}$ is the prescribed traction of the fluid phase.

Similarly, the weak form of the Poisson equation for the pore pressure increment is as below:

$$\int_{\Omega_t}\delta p\ \Delta t\left(\frac{\theta_s}{\rho_s}+\frac{\theta_f}{\rho_f}\right)\nabla_x^2(\Delta p^{t+1})d\Omega=\int_{\Omega_t}\delta p\ \theta_s\nabla_x\cdot\boldsymbol{v}_s^*d\Omega+\int_{\Omega_t}\delta p\ \theta_f\nabla_x\cdot\boldsymbol{v}_f^*d\Omega\tag{33}$$

where δp is the test function for pore pressure, and it is assumed to be zero at the pore pressure boundary conditions $\partial\Omega^p$.

Since the external loadings are already enforced during the prediction stage Equations (31) and (32), the solid and fluid phases can be considered together to update the kinematic variables. The corresponding weak forms are presented as follows:

$$\int_{\Omega_t}\delta\boldsymbol{v}\cdot\left(\theta_s\rho_s\boldsymbol{a}_s^{**}\right)d\Omega_t=-\int_{\Omega_t}\delta\boldsymbol{v}\cdot\theta_s\nabla_x(\Delta p^{t+1})d\Omega_t\tag{34}$$

$$\int_{\Omega_t}\delta\boldsymbol{v}\cdot\left(\theta_f\rho_f\boldsymbol{a}_f^{**}\right)d\Omega_t=-\int_{\Omega_t}\delta\boldsymbol{v}\cdot\theta_f\nabla_x(\Delta p^{t+1})d\Omega_t\tag{35}$$

3 | Total Lagrangian MPM for Hydromechanical Coupling Analysis

3.1 | Total Lagrangian Formulation

To develop the TLMPM for hydromechanical coupling analysis, it is essential to reformulate the weak form of the governing Equations (2.7) into their Total Lagrangian form that is established with respect to the reference configuration, as shown in Figure 2.

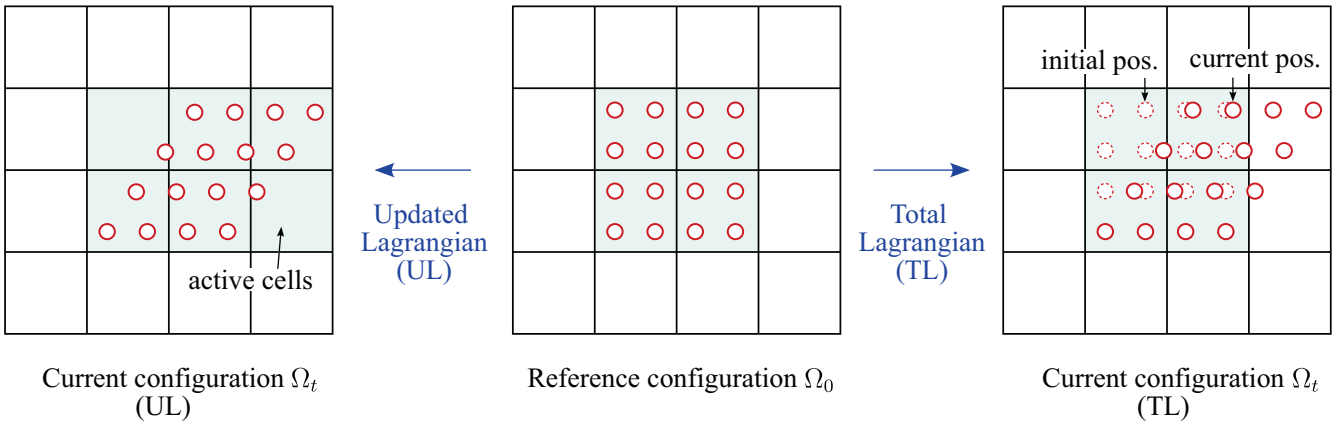

FIGURE 2 | Comparison of Total Lagrangian (TL) MPM and Updated Lagrangian (UL) MPM. The shaded region indicates the activated cell when using standard MPM shape functions.

3.1.1 | Prediction Stage

Firstly, we can obtain the Total Lagrangian weak form of momentum equation for the mixture by pulling back Equation (31) and making use of $\frac{1}{J}\nabla_X \cdot (J\boldsymbol{\sigma}\boldsymbol{F}^{-T}) = \nabla_x \cdot \boldsymbol{\sigma}$, which yields to:

$$\int_{\Omega_0} \delta\boldsymbol{v} \cdot \left(\theta_s \rho_s \boldsymbol{a}_s^* J^t\right) d\Omega_0 + \int_{\Omega_0} \delta\boldsymbol{v} \cdot \left(\theta_f \rho_f \boldsymbol{a}_f^* J^t\right) d\Omega_0 = -\int_{\Omega_0} \nabla_X \delta\boldsymbol{v} : \left(\boldsymbol{P}'^{,t} - p^t J^t \boldsymbol{F}^{-T}\right) d\Omega_0 + \int_{\Omega_0} \delta\boldsymbol{v} \cdot \rho\boldsymbol{b} J^t d\Omega_0 + \int_{\partial\Omega_0^\tau} \delta\boldsymbol{v} \cdot \boldsymbol{T} dS_0 \tag{36}$$

where Ω_0 refers to the reference configuration, $\boldsymbol{T} = \boldsymbol{P}^t \cdot \boldsymbol{N}$ is the first Piola–Kirchhoff traction vector acting on the mixture, and $\boldsymbol{N}$ is the outward unit normal vector to the boundary surface $\partial\Omega_0$.

For ease of constructing the Total Lagrangian formulation for the fluid phase, which involves the drag force term, we invoke the Kozeny–Carman equation [50, 51] to relate the current permeability to the initial permeability in the reference configuration k_0, which is given below:

$$k^t = \frac{\left(\theta_f^t\right)^3}{\left(1-\theta_f^t\right)^2}\kappa \equiv \frac{\left(\theta_f^t\right)^3}{\left(\theta_f^0\right)^3}\frac{\left(1-\theta_f^0\right)^2}{\left(1-\theta_f^t\right)^2}k^0 \equiv \frac{\left(\theta_f^t\right)^3}{\left(\theta_f^0\right)^3}\frac{\left(\theta_s^0\right)^2}{\left(\theta_s^t\right)^2}k^0 \equiv \frac{\left(\theta_f^t\right)^3}{\left(\theta_f^0\right)^3}(J^t)^2 k^0 \tag{37}$$

where κ is the reference permeability coefficient, which is assumed to be constant and a function of grain size distribution, shape, and roughness. With Equation (37) in hand, and by invoking Equation (16), the Total Lagrangian weak form for the fluid phase can be expressed as:

$$\int_{\Omega_0} \delta\boldsymbol{v} \cdot \left(\theta_f^t \rho_f \boldsymbol{a}_f^*\right) J^t d\Omega_0 = \int_{\Omega_0} \theta_f^t \nabla_X \delta\boldsymbol{v} : \left(J^t p^t \boldsymbol{F}^{-T}\right) d\Omega_0 - \int_{\Omega_0} \delta\boldsymbol{v} \cdot \left(\frac{\left(\theta_f^0\right)^3}{J^t - 1 + \theta_f^0}\frac{\rho_f g}{k^0}\left(\boldsymbol{v}_f^* - \boldsymbol{v}_s^*\right)\right) d\Omega_0 + \int_{\Omega_0} \delta\boldsymbol{v} \cdot \theta_f^t \rho_f \boldsymbol{b}\, J^t d\Omega_0 + \int_{\partial\Omega_0^p} \delta\boldsymbol{v} \cdot \boldsymbol{T}_f dS_0 \tag{38}$$

where $\boldsymbol{T}_f = -\left(\theta_f^t \bar{p} J^t \boldsymbol{F}^{-T}\right) \cdot \boldsymbol{N}$ is the first Piola–Kirchhoff traction vector acting on the fluid phase pore-pressure boundary $\partial\Omega_0^p$.

3.1.2 | Pore Pressure Solution

To simplify the derivation, we denote $\eta^t = \Delta t\left(\frac{\theta_s^t}{\rho_s} + \frac{\theta_f^t}{\rho_f}\right)$. By transforming the integration domain from Ω_t to Ω_0, we can arrange Equation (33) as follows:

$$\int_{\Omega_0} \delta p\ \eta^t \nabla_x^2(\Delta p^{t+1}) J^t d\Omega_0 = \int_{\Omega_0} \delta p\ \theta_s^t \nabla_x \cdot \boldsymbol{v}_s^*\ J^t d\Omega_0 + \int_{\Omega_0} \delta p\ \theta_f^t \nabla_x \cdot \boldsymbol{v}_f^*\ J^t d\Omega_0 \tag{39}$$

Applying integration by parts and divergence theorem, the *LHS* of Equation (39) can be written as:

$$\int_{\Omega_0} \delta p\ \eta^t \nabla_x^2(\Delta p^{t+1}) J^t d\Omega_0 = -\int_{\Omega_0} \eta^t J^t \nabla_x \delta p \cdot \nabla_x(\Delta p^{t+1}) d\Omega_0 + \int_{\partial\Omega_0^v} \delta p\ T_p\ dS_0 \tag{40}$$

Here, $T_p = \eta^t J^t \nabla_x(\Delta p^{t+1}) \cdot \boldsymbol{N}$ denotes the spatial pressure gradient traction acting on the reference pressure Neumann boundary $\partial\Omega_0^v$. In the present work, the problems considered involve boundary conditions where this term vanishes (e.g., homogeneous Neumann boundary conditions with no inflow or outflow fluxes, as well as Dirichlet pressure conditions at the free surface, $p = 0$ on Γ_p, and homogenous kinematic boundary, $\boldsymbol{v}_\alpha \cdot \boldsymbol{n} = 0$ on Γ_u). For such cases, Equation (39) simplifies to:

$$\int_{\Omega_0} \eta^t \nabla_x \delta p \cdot \nabla_x(\Delta p^{t+1}) J^t d\Omega_0 = -\int_{\Omega_0} \delta p\ \theta_s^t \nabla_x \cdot \boldsymbol{v}_s^* J^t d\Omega_0 - \int_{\Omega_0} \delta p \theta_f \nabla_x \cdot \boldsymbol{v}_f^* J^t d\Omega_0 \tag{41}$$

Considering the following identity for any scalar field ϕ and vector field $\boldsymbol{u}$ [52]:

$$\nabla_x \phi = \boldsymbol{F}^{-T} \nabla_X \phi \tag{42}$$

$$\nabla_x \cdot \boldsymbol{u} = \frac{1}{J} \nabla_X \cdot \left(J \boldsymbol{F}^{-1} \boldsymbol{u}\right) \tag{43}$$

we could finally obtain the Total Lagrangian weak form of the Poisson equation for pore pressure:

$$\begin{aligned} \int_{\Omega_0} \eta^0 \left(\boldsymbol{F}^{-T} \nabla_X \delta p\right) \cdot \left(\boldsymbol{F}^{-T} \nabla_X(\Delta p^{t+1})\right)\ d\Omega_0 = &-\int_{\Omega_0} \delta p\ \theta_s^t \nabla_X \cdot \left(J^t \boldsymbol{F}^{-1} \boldsymbol{v}_s^*\right) d\Omega_0 \\ &-\int_{\Omega_0} \delta p\ \theta_f^t \nabla_X \cdot \left(J^t \boldsymbol{F}^{-1} \boldsymbol{v}_f^*\right) d\Omega_0 \end{aligned} \tag{44}$$

where through Equation (16), we can express

$$\eta^0 = \Delta t\left(\frac{\theta_s^0}{\rho_s} + \frac{J^t - 1 + \theta_f^0}{\rho_f}\right) \tag{45}$$

3.1.3 | Correction Stage

The Total Lagrangian weak form of the momentum equation for the correction stage is derived similarly to the prediction stage and can be expressed as follows:

$$\int_{\Omega_0} \delta \boldsymbol{v} \cdot \left(\theta_s^t \rho_s \boldsymbol{a}_s^{**} J^t\right) d\Omega_0 = -\int_{\Omega_0} \delta \boldsymbol{v} \cdot \theta_s^t \boldsymbol{F}^{-T} \nabla_X(\Delta p^{t+1}) J^t d\Omega_0 \tag{46}$$

$$\int_{\Omega_0} \delta \boldsymbol{v} \cdot \left(\theta_f^t \rho_f \boldsymbol{a}_f^{**} J^t\right) d\Omega_0 = -\int_{\Omega_0} \delta \boldsymbol{v} \cdot \theta_f^t \boldsymbol{F}^{-T} \nabla_X(\Delta p^{t+1}) J^t d\Omega_0 \tag{47}$$

3.2 | Discretization

In MPM discretization, the continuous volume integral is approximated by a finite number of material points:

$$\int_{\Omega_0}(\square)d\Omega \approx \sum_{p=1}^{n_p}\int_{\Omega_p^0}(\square)d\Omega_p = \sum_{p=1}^{n_p}(\square)V_p^0 \tag{48}$$

where n_p denotes the number of material points, and V_p^0 represents the undeformed volume of the material point. Following the Generalized Interpolation Material Point Method (GIMP) [53], we define the weighting function as follows:

$$S_{Ip} \equiv S_I(\boldsymbol{X}_p) = \frac{1}{V_p}\int_{\Omega_p\cap\Omega}\chi_p(\boldsymbol{x})N_I(\boldsymbol{x})d\Omega \tag{49}$$

$$\nabla S_{Ip} \equiv \nabla_X S_I(\boldsymbol{X}_p) = \frac{1}{V_p}\int_{\Omega_p\cap\Omega}\chi_p(\boldsymbol{x})\nabla N_I(\boldsymbol{x})d\Omega \tag{50}$$

where χ_p and $N_I(\boldsymbol{x})$ are the particle characteristic function and the grid shape function, respectively. For convenience, the same interpolation function will be used for both displacement and pressure discretization, which is written as:

$$\boldsymbol{a}_{\alpha p} = \sum_{I=1}^{n_n} S_{Ip}\boldsymbol{a}_{\alpha I}, \quad \boldsymbol{v}_{\alpha p} = \sum_{I=1}^{n_n} S_{Ip}\boldsymbol{v}_{\alpha I}, \quad p_p = \sum_{I=1}^{n_n} S_{Ip}p_I \tag{51}$$

where n_n is the number of node connectivity.

It is worth noting that, in the presented TLMPM, the weighting function is evaluated only once in the undeformed configuration and remains unchanged throughout the simulation process. This feature offers a notable advantage compared to the conventional ULMPM, as it eliminates the need for repeated material point tracking and basis function recalculation, thereby significantly reducing the computational cost. Additionally, the particle volume in Equations (49) and (50) is taken as V_p^0.

3.2.1 | Prediction Stage

Substituting Equations (51) into (36) and (38), the split momentum equation at the prediction stage can be rewritten as the following matrix form:

$$\begin{bmatrix} \mathcal{M}_s & \mathcal{M}_f \\ -\Delta t\mathcal{Q} & \mathcal{M}_f + \Delta t\mathcal{Q} \end{bmatrix}\begin{Bmatrix} \boldsymbol{a}_s^* \\ \boldsymbol{a}_f^* \end{Bmatrix} = \begin{Bmatrix} \boldsymbol{f}^{\text{int}} + \boldsymbol{f}^{\text{ext}} \\ \boldsymbol{f}_f^{\text{int}} + \boldsymbol{f}_f^{\text{ext}} - \mathcal{Q}(\boldsymbol{v}_f^t - \boldsymbol{v}_s^t) \end{Bmatrix} \tag{52}$$

in which:

$$(\mathcal{M}_s)_{IJ} = \sum_{p=1}^{n_p} m_{sp}S_{Ip}S_{Jp}, \quad m_{sp} = \theta_{sp}^0\rho_s V_p^0 \tag{53}$$

$$(\mathcal{M}_f)_{IJ} = \sum_{p=1}^{n_p}\left(J_p^t - 1 + \theta_{fp}^0\right)\rho_f S_{Ip}S_{Jp}V_p^0 \tag{54}$$

$$\mathcal{Q}_{IJ} = \sum_{p=1}^{n_p}\frac{\left(\theta_{fp}^0\right)^3}{J_p^t - 1 + \theta_{fp}^0}\frac{\rho_f g}{k^0}S_{Ip}S_{Jp}V_p^0 \tag{55}$$

$$(\boldsymbol{f}^{\text{int}})_I = -\sum_{p=1}^{n_p}\nabla_X S_{Ip} : \left(\boldsymbol{P}_p'^{\,t} - p_p^t J_p^t \boldsymbol{F}_p^{-T}\right)V_p^0 \tag{56}$$

$$(\boldsymbol{f}^{\text{ext}})_I = \sum_{p=1}^{n_p}(m_{fp} + m_{sp})\boldsymbol{b}S_{Ip} + \int_{\partial\Omega_0} S_{Ip}\boldsymbol{T}\, dS_0 \tag{57}$$

$$\left(\boldsymbol{f}_f^{\text{int}}\right)_I = \sum_{p=1}^{n_p}\nabla_X S_{Ip} : \left(\left(J_p^t - 1 + \theta_{fp}^0\right)p_p^t\boldsymbol{F}_p^{-T}\right)V_p^0 \tag{58}$$

$$\left(\boldsymbol{f}_f^{\text{ext}}\right)_I = \sum_{p=1}^{n_p} m_{fp}\boldsymbol{b}S_{Ip} + \int_{\partial\Omega_0} S_{Ip}\boldsymbol{T}_f\, dS_0 \tag{59}$$

It is worth noting that the coefficient matrix in Equation (52) is non-symmetric, which typically necessitates the use of specialized solvers, such as the least-squares conjugate gradient (LSCG) method, to resolve the system. To enhance computational efficiency and stability, we can rearrange Equation (52) by subtracting the second row from the first row to obtain a symmetric coefficient matrix. This treatment could enable the use of more efficient solvers and, more importantly, make it compatible with Cholesky factorization as will be discussed later.

$$\begin{bmatrix} \mathcal{M}_s + \Delta t\mathcal{Q} & -\Delta t\mathcal{Q} \\ -\Delta t\mathcal{Q} & \mathcal{M}_f + \Delta t\mathcal{Q} \end{bmatrix} \begin{Bmatrix} \boldsymbol{a}_s^* \\ \boldsymbol{a}_f^* \end{Bmatrix} = \begin{Bmatrix} \boldsymbol{f}^{\text{int}} + \boldsymbol{f}^{\text{ext}} - \left(\boldsymbol{f}_f^{\text{int}} + \boldsymbol{f}_f^{\text{ext}} - \mathcal{Q}(\boldsymbol{v}_f^t - \boldsymbol{v}_s^t) \right) \\ \boldsymbol{f}_f^{\text{int}} + \boldsymbol{f}_f^{\text{ext}} - \mathcal{Q}(\boldsymbol{v}_f^t - \boldsymbol{v}_s^t) \end{Bmatrix} \tag{60}$$

In most existing MPM implementations, the consistent mass matrix $\mathcal{M}_\alpha$ is commonly approximated by a lumped mass matrix. This approximation is achieved by summing the entries of each row of the consistent mass matrix into its diagonal components, utilizing the property of the weight function, $\sum_{J=1}^{n_n} S_J = 1$ (cf. Figure 3). The resulting lumped mass matrix is given by the following expression, where repeated indices do not imply Einstein summation:

$$\left(\mathcal{M}_\alpha\right)_{IJ} = \sum_{p=1}^{n_p} m_{\alpha p} S_{Ip} \delta_{IJ} \tag{61}$$

In explicit MPM, the lumped mass is typically preferred because its diagonal structure enables a straightforward explicit update and enhances computational efficiency. In UL semi-implicit MPM, a lumped mass matrix is often effectively required. As the particles move above the background mesh, the evolving shape functions can result in poorly conditioned off-diagonal terms in the consistent mass matrix, and thus causing instability and premature termination. By contrast, TL semi-implicit MPM adopts shape functions in the reference configuration, avoiding such issues in the consistent mass matrix structure. Since the consistent mass matrix better preserves the coupling between degrees of freedom (DOFs) in the discretized system and generally provides higher accuracy, it is adopted as the default choice in our TL MPM formulation.

3.2.2 | Pore Pressure Solution

After obtaining the intermediate accelerations of the nodes, the next step is to solve the Poisson equation for the pressure increment. After discretization, the Poisson equation for the pore pressure can be written in matrix form as below:

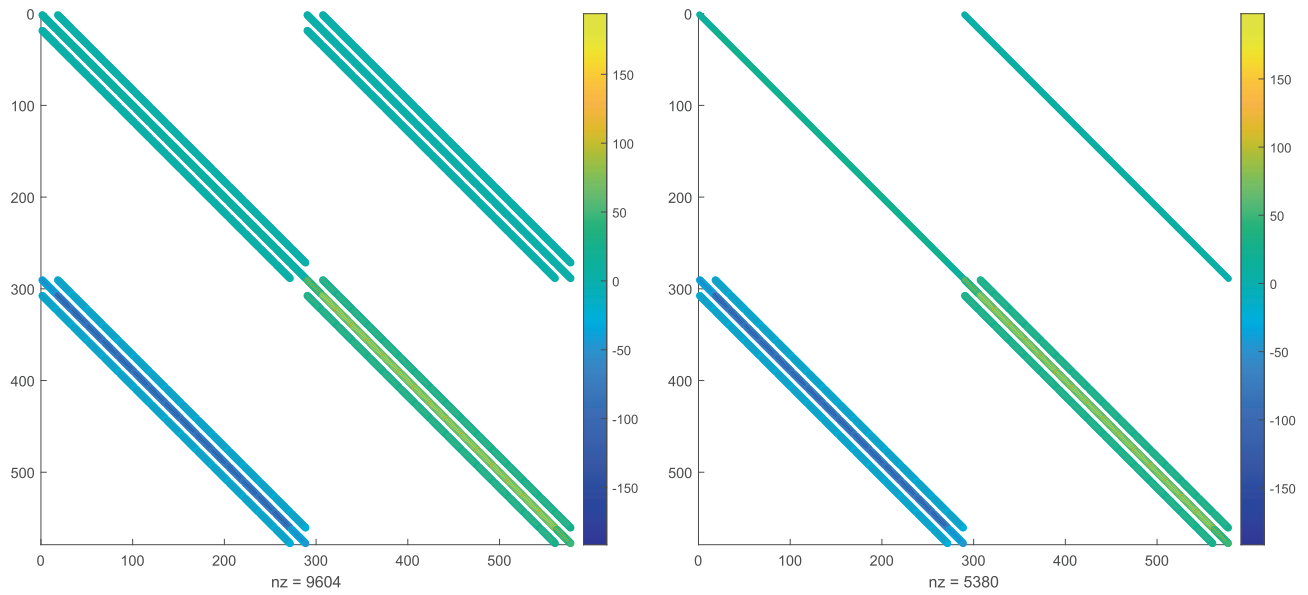

(a) With consistent mass matrix block (b) With lumped mass matrix block

FIGURE 3 | Sparsity pattern for coefficient matrix in prediction stage (Equation (52)). (a) With a consistent mass matrix block, (b) With a lumped mass matrix block.

$$\mathcal{L}\{\Delta \boldsymbol{p}\} = \boldsymbol{c} \tag{62}$$

with:

$$\mathcal{L}_{IJ} = \Delta t \sum_{p=1}^{n_p} \left(\frac{\theta_{sp}^0}{\rho_s} + \frac{J_p^t - 1 + \theta_{fp}^0}{\rho_f} \right) V_p^0 \nabla S_{Ip}^T \boldsymbol{B}_p \nabla S_{Jp} \tag{63}$$

$$\Delta p_J = p_J^{t+1} - p_J^t \tag{64}$$

$$\begin{aligned} c_I = & \sum_{J=1}^{n_n} \sum_{p=1}^{n_p} \left((J_p^t - 1 + \theta_{fp}^0) V_p^0 \nabla_X S_{Ip}^T \boldsymbol{F}_p^{-T} S_{Jp} \right) \boldsymbol{v}_{fJ}^* \\ & + \sum_{J=1}^{n_n} \sum_{p=1}^{n_p} \left(\theta_{sp}^0 V_p^0 \nabla_X S_{Ip}^T \boldsymbol{F}_p^{-T} S_{Jp} \right) \boldsymbol{v}_{sJ}^* \end{aligned} \tag{65}$$

where $\boldsymbol{B}$ is the so-called Piola deformation tensor, defined as the inverse of the right Cauchy-Green tensor, that is, $\boldsymbol{B} = \boldsymbol{C}^{-1}$ with $\boldsymbol{C}^{-1} = (\boldsymbol{F}^T \ \boldsymbol{F})^{-1} = \boldsymbol{F}^{-1}\boldsymbol{F}^{-T}$.

3.2.3 | Correction Stage

Once the nodal pressure increment is obtained, we proceed to discretize the momentum equations for the correction stage, as presented in Equations (46) and (47). These equations can be expressed in matrix form as follows:

$$\begin{bmatrix} \mathcal{M}_s & \boldsymbol{0} \\ \boldsymbol{0} & \mathcal{M}_f \end{bmatrix} \begin{Bmatrix} \boldsymbol{a}_s^{**} \\ \boldsymbol{a}_f^{**} \end{Bmatrix} = \begin{Bmatrix} \mathcal{G}_s \Delta \boldsymbol{p} \\ \mathcal{G}_f \Delta \boldsymbol{p} \end{Bmatrix} \tag{66}$$

where the mass matrix $\mathcal{M}_s$ and $\mathcal{M}_f$ is given in the same form as Equations (53) and (54), while the entity of matrices $\mathcal{G}_s$ and $\mathcal{G}_f$ are given as:

$$\left(\mathcal{G}_s\right)_{IJ} = -\sum_{p=1}^{n_p} \theta_s^0 S_{Ip} \boldsymbol{F}_p^{-T} \nabla_X S_{Jp} V_p^0 \tag{67}$$

$$\left(\mathcal{G}_f\right)_{IJ} = -\sum_{p=1}^{n_p} \left(J_p^t - 1 + \theta_{fp}^0 \right) S_{Ip} \boldsymbol{F}_p^{-T} \nabla_X S_{Jp} V_p^0 \tag{68}$$

If the lumped-mass matrix is considered, Equation (66) can be solved explicitly, that is, via the mapped nodal mass, thereby eliminating the need for matrix inversion.

4 | Numerical Implementation

4.1 | Critical Time Step

For the explicit MPM, the critical time step is constrained jointly by the Courant-Friedrichs-Lewy (CFL) condition [54] and the permeability of the porous medium [55], which is given by:

$$\Delta t_{crit} = \min\left(\frac{\Delta h_e}{c^p}, -\frac{1}{\omega^2} \left(\frac{\rho_f g}{\rho^m k} + \sqrt{\left(\frac{\rho_f g}{\rho^m k} \right)^2 + 4\omega^2} \right) \right) \tag{69}$$

In the above expression, the first term represents the CFL condition, while the second term denotes the permeability-related constraint. Here, Δh_e is the element size, c^p is the compressional wave velocity in the porous medium, and $\omega^2 = 4E/\left(\rho^m \Delta h_e^2\right)$, where $\rho^m = \rho + \left(1/\theta_f - 2\right)\rho_f$ is the modified mixture density. The parameters E, k, and $\rho = \theta_s \rho_s + \theta_f \rho_f$ represent the elastic modulus of the solid phase, permeability, and bulk mixture density, respectively.

In the two-phase explicit MPM implementation [20], the fluid is assumed to be weakly compressible, and its pressure is obtained explicitly via the volume change. Therefore, in applying the CFL condition in Equation (69), the compressional wave velocity of the pore fluid phase should be used, which is given by:

$$c^p = c_f^p = \sqrt{\frac{K_f}{\rho_f}} \tag{70}$$

where K_f is the bulk modulus of the fluid phase.

In our previously proposed UL semi-implicit MPM [26], the pore pressure is computed implicitly while stress integration for the solid phase and the evaluation of internal forces are performed explicitly at the current configuration time t. Thus, the CFL condition is still required for maintaining numerical stability. However, in contrast to the explicit counterpart, the wave velocity used for the CFL condition in the semi-implicit scheme can be based on the wave velocity of the solid skeleton, which is generally lower than the wave speed of the compressible fluid phase alone. This wave velocity is given by:

$$c^p = \sqrt{\frac{K_s + 4G/3}{\rho_s \theta_s}} \tag{71}$$

where K_s and G are the bulk modulus and shear modulus of the solid phase.

This distinction in wave speed selection between the explicit and semi-implicit formulations leads to a less restrictive CFL condition in the semi-implicit MPM, and hence a larger permissible critical time step. Furthermore, due to the drag force term is treated implicitly, the semi-implicit scheme also allows for a permeability-independent time step [26], which is more advantageous in low-permeability scenarios.

4.2 | Numerical Approximation and Factorization

As discussed in Section 3, solving linear systems of equations is a critical computational task in the proposed TLMPM. Up to three linear systems must be solved at each time step (reduced to two when a lumped mass matrix is employed), and these systems, despite having different sets of unknowns, can generally be expressed as:

$$\boldsymbol{\mathcal{A}}^t \boldsymbol{x}^t = \boldsymbol{b}^t \tag{72}$$

where $\boldsymbol{\mathcal{A}}^t$ is the coefficient matrix, $\boldsymbol{x}^t$ is the vector of unknowns, and $\boldsymbol{b}^t$ is the RHS vector. Given the restriction on small time steps (see Section 4.1), achieving computational efficiency in solving these systems is imperative.

Efficiency improvements can be realized by exploiting the characteristics of the coefficient matrices within TLMPM. In this formulation, the shape functions and their gradients are evaluated at the *initial* positions of the particles. As a result, both their values and the connectivity between particles and nodes remain unchanged during the computation. Consequently, the size and sparsity patterns of the coefficient matrices $\boldsymbol{\mathcal{A}}^t$ Equations (60), (62), and (66) are preserved throughout the simulation. Although some components of the coefficient matrix, for example, $\boldsymbol{J}_p^t$ and $\boldsymbol{B}_p^t$, may vary with time due to material deformation and fluid flow, these changes are typically gradual under the small time step condition. This observation motivates approximating the coefficient matrix as constant over multiple time steps, with updates occurring at regular intervals, that is, $n_k \Delta t$. Thus, we approximate $\boldsymbol{\mathcal{A}}^t$ as follows:

$$\boldsymbol{\mathcal{A}}^t \approx \widetilde{\boldsymbol{\mathcal{A}}} = \boldsymbol{\mathcal{A}}^{t_k}, \quad \text{for } t_k \le t < t_{k+1} \tag{73}$$

where $\widetilde{\boldsymbol{\mathcal{A}}}$ denotes the approximated coefficient matrix, t_k is the time when the matrix was last updated, and $t_{k+1} = t_k + n_k \Delta t$ is the subsequent update time. By assuming $\boldsymbol{\mathcal{A}}$ remains constant within $[t_k, t_{k+1})$, we can achieve substantial computational savings by avoiding the matrix assembly at each time step. More importantly, the factorization of $\boldsymbol{\mathcal{A}}^t$ can be precomputed at time t_k and subsequently reused for solving the linear systems in Equation (72) over the entire interval.

Because all relevant matrices are symmetric and positive definite, a Cholesky decomposition is particularly advantageous. In this approach, the approximate coefficient matrix is decomposed as:

$$\widetilde{\boldsymbol{\mathcal{A}}} = \boldsymbol{\mathcal{A}}_L \boldsymbol{\mathcal{A}}_L^T \tag{74}$$

where $\mathcal{A}_L$ is a lower triangular matrix (see the example in Figure 4). This decomposition facilitates the efficient solution of the linear system $\widetilde{\mathcal{A}}\boldsymbol{x}^t = \boldsymbol{b}^t$ by performing two steps:

$$\mathcal{A}_L \boldsymbol{y} = \boldsymbol{b}^t, \quad \text{forward substitution} \tag{75}$$

$$\mathcal{A}_L^T \boldsymbol{x}^t = \boldsymbol{y}, \quad \text{backward substitution} \tag{76}$$

where $\boldsymbol{y}$ denotes an auxiliary vector of intermediate unknowns. Compared to LU decomposition, Cholesky decomposition provides approximately twice the computational efficiency [56]. Although the decomposition itself has a time complexity of $\mathcal{O}(n^3)$, comparable to that of directly computing $\widetilde{\mathcal{A}}^{-1}$, the subsequent solution of the triangular systems requires only $\mathcal{O}(n^2)$ operations. This is in contrast to the $\mathcal{O}(n^3)$ operations normally required for full matrix multiplication, such as computing $\widetilde{\mathcal{A}}^{-1}\boldsymbol{b}^t$. These efficiency gains become increasingly significant as the matrix size grows.

In contrast, the traditional ULMPM requires the evaluation of shape functions and their gradients based on the *current* positions of material points. Consequently, these functions and their gradients, along with the associated properties, evolve dynamically over time. Moreover, material points may occasionally traverse computational cells, altering the active degrees of freedom (DOFs), the node-material-point connectivity, and the underlying system matrix pattern. As a result, the system matrices must be reassembled at each time step, thereby precluding any computational savings that might otherwise be realized from the numerical approximations or matrix factorizations described above. This requirement significantly increases both the computational cost and the overall methodological complexity.

4.3 | Pore Pressure Stabilization

While the fractional step method effectively reduces pressure oscillations caused by equally low-order interpolations for pressure and kinematic fields, these oscillations may still persist when using significantly small time steps [57, 58]. In our original implementation of FSM [26], we proposed the straightforward pore pressure smoothing technique to mitigate these oscillations. However, it often introduces excessive numerical dissipation in the computed pressure field and compromises the accuracy of analyses. For this reason, we do not adopt the smoothing technique in the present study.

To further alleviate the effects of inf-sup instability, we employ an alternative stabilization approach known as the polynomial pressure projection (PPP) method [32, 59–60]. This method introduces a penalty term to the mass balance equation,

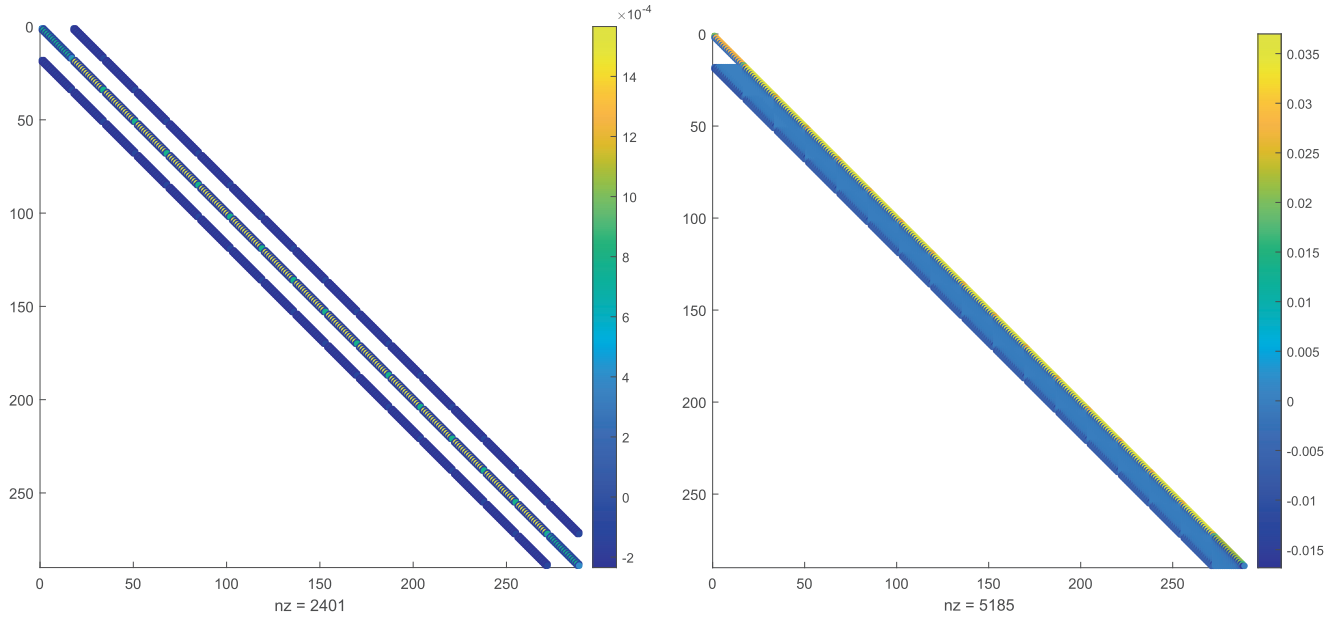

(a) Without Cholesky decomposition (b) Lower triangular factor for Cholesky decomposition

FIGURE 4 | Sparsity pattern for coefficient matrix in Poisson equation (Equation 62). (a) Without Cholesky decomposition, (b) Lower triangular factor for Cholesky decomposition.

thereby ensuring that the overall system satisfies a weak inf-sup condition. In the context of the FSM, the modified pressure Poisson equation is formulated as follows:

$$(\boldsymbol{\mathcal{L}} + \boldsymbol{\mathcal{H}}_{\text{stab}})\{\Delta \boldsymbol{p}\} = \boldsymbol{c} \tag{77}$$

where $\boldsymbol{\mathcal{H}}_{\text{stab}}$ is the stabilization matrix defined by:

$$(\boldsymbol{\mathcal{H}}_{\text{stab}})_{IJ} = \sum_{p=1}^{n_p} \frac{\tau}{2G\Delta t}\left(S_{Ip}^{\mathrm{T}} - S_{avg}^{\mathrm{T}}\right)\left(S_{Ip} - S_{avg}\right) J^t V_p^0 \tag{78}$$

Here, S_{avg} denotes the averaged weighting function, which can be easily evaluated as $1/n_{nnpe}$ with n_{nnpe} being the number of nodes per element, G is the shear modulus of the solid material, and τ is the stabilization parameter. It is important to note that if τ is chosen too large, excessive numerical diffusion may smear pressure gradients as stated by [59]; if it is too small, stabilization becomes ineffective and spurious pressure modes can persist (see an example in Section B). Therefore, it is crucial to select an appropriate τ for effective stabilization. In our experience, setting τ to the identity provides a robust starting point that balances stability and diffusion across a broad range of cases. For further guidance on determining τ, readers are referred to [60].

4.4 | Boundary Conditions

Boundary conditions (BCs) play a crucial role in numerically resolving the coupled hydromechanical system. For BCs of the kinematic fields (both Dirichlet and Neumann types) and the Neumann BCs of the pore pressure field, there is negligible difference between the ULMPM and TLMPM implementations, as the corresponding boundary node sets are generally predefined either in the current or reference configurations.[1] During computation, these constraints are enforced in the matrix equations through direct modifications of matrices or penalty methods.

However, there are significant differences between the two approaches in enforcing Dirichlet boundary conditions for the pore pressure field. In ULMPM, the continuous movement and deformation of the free surface boundary make it impossible to predefine the sets of boundary nodes near the free surface. Thus, an additional free-surface detection algorithm is required to dynamically detect the evolution of the free surface at each time step, providing constraints to the Poisson equation. A widely adopted technique for free surface detection employs a volume-fraction-based criterion inspired by the Volume of Fluid (VOF) method [37]. Specifically for ULMPM simulations presented in this work, we modified the volume-fraction-based method, which was originally proposed for cell-based evaluation, to node-based evaluation. Here, we compute the volume fraction α_I for all nodes:

$$\alpha_I = \frac{1}{V_e}\sum_{p=1}^{n_p} S_{Ip} V_p \tag{79}$$

where V_e is the cell volume (for a regular mesh). If the computed volume fraction falls below a threshold ϵ_n and the node does not belong to other sets of BCs, those nodes are identified as free-surface nodes. It should be noted that the choice of this threshold may depend on the dimension of the problem and the selection of the shape function. In the current study, we used $\epsilon_n = 0.8$ for UL-MPM and $\epsilon_n = 0.25$ for UL-GIMP. However, as recently discussed by [36], the imposition of the free-surface boundary condition on the background grid nodes, rather than at the actual material boundary, can lead to numerical pressure oscillations, which may lead to numerical instabilities.

On the other hand, the proposed TLMPM offers the desired ease in the enforcement of Dirichlet boundary conditions for pore pressure. Since the deformations are mapped back to the fixed reference configuration where the matrix equation is established, the free surface nodes are easily identified and can be predefined at the beginning of the simulation. This simplification facilitates the implementation and reduces computational costs since the global matrix structure remains consistent and valid throughout the analysis. A detailed comparison between the ULMPM and TLMPM approaches for handling boundary conditions is provided in Section 5.4.

4.5 | Computational Procedure

In this section, we present the detailed computational procedure employed in our implementation. Following the Update Stress First (USF) scheme, the procedure consists of four key steps described in the subsequent subsections.

4.5.1 | Particle-to-Grid Mapping (P2G)

At the beginning of each time step, the mass and momentum of each constituent of material points are mapped onto the background computational grid, expressed as:

$$m_{\alpha I} = \sum_{p=1}^{n_p} S_{Ip} m_{\alpha p} \tag{80}$$

$$(m\boldsymbol{v})^t_{\alpha I} = \sum_{p=1}^{n_p} S_{Ip} m_{\alpha p} \boldsymbol{v}^t_{\alpha p} \tag{81}$$

Because the TL formulation is adopted, the nodal mass is computed only once at the beginning of the simulation. The nodal velocity can then be computed as:

$$\boldsymbol{v}^t_{\alpha I} = \frac{(m\boldsymbol{v})^t_{\alpha I}}{m_{\alpha I}} \tag{82}$$

4.5.2 | Deformation and Stress Update

Once the particle data have been transferred to the grid, the deformation gradient at each material point is updated based on the current velocity field, which is given by:

$$\boldsymbol{F}^{t+1} = \frac{\partial \boldsymbol{x}^{t+1}}{\partial X} = \frac{\partial \left(\boldsymbol{x}^t + \Delta \boldsymbol{u}\right)}{\partial \boldsymbol{X}} = \boldsymbol{F}^t + \Delta t \frac{\partial \boldsymbol{v}}{\partial \boldsymbol{X}} = \boldsymbol{F}^t + \Delta t \sum_{I=1}^{n_n} \nabla_X S_{Ip} v^t_{sI} \tag{83}$$

It is worth noting that this expression differs slightly from the form commonly used in the UL formulation:

$$\boldsymbol{F}^{t+1} = \frac{\partial \boldsymbol{x}^{t+1}}{\partial X} = \frac{\partial \boldsymbol{x}^{t+1}}{\partial \boldsymbol{x}^t} \frac{\partial \boldsymbol{x}^t}{\partial \boldsymbol{X}} = \frac{\partial \left(\boldsymbol{x}^t + \boldsymbol{v}\Delta t\right)}{\partial \boldsymbol{x}^t} \frac{\partial \boldsymbol{x}^t}{\partial \boldsymbol{X}} = \left(\boldsymbol{I} + \Delta t \sum_{I=1}^{n_n} \nabla_x S^t_{Ip} v^t_{sI} \right) \boldsymbol{F}^t \tag{84}$$

With the updated deformation gradient available, the stress at each material point is then computed using the appropriate constitutive model, such as the Neo–Hookean model detailed in Section 2.3.

4.5.3 | Nodal Solution

After updating the deformation and stress in each material point, the next step involves solving the momentum equation and the pore pressure Poisson equation on the background mesh. This includes solving the split momentum equation, computing the intermediate acceleration (or velocity) in Equation (60), solving the nodal pore pressure increment in Equation (62), and finally updating the nodal kinematics in Equation (66). It should be noted that a Cholesky decomposition is performed at regular intervals to efficiently accelerate the matrix solution process, as detailed in Section 4.2.

4.5.4 | Grid-to-Particle Mapping (G2P)

At the end of each step, the updated nodal quantities are transferred back to material points to update their positions and velocities:

$$\boldsymbol{x}^{t+1}_p = \boldsymbol{x}^t_p + \Delta t \sum_{I=1}^{n_n} S_{Ip} \boldsymbol{v}^{t+1}_{sI} \tag{85}$$

$$\boldsymbol{v}^{t+1}_{\alpha p} = \boldsymbol{v}^t_{\alpha p} + \Delta t \sum_{I=1}^{n_n} S_{Ip} \boldsymbol{a}^{t+1}_{\alpha I} \tag{86}$$

Here, the FLIP scheme is employed for the velocity update due to its better energy conservation properties compared to PIC.

ALGORITHM 1 | TLMPM.

```
if t = 0 then
   Compute particle volume V_p^0, volume fraction θ_αp^0, particle mass m_αp^0, shape function
S_Ip and its gradient ∇S_Ip
   Identify the boundary node set
end if
while t ≤ t_end do
   if t = t_k then
      Assemble coefficient matrix in Equations (60), (62), and (66)
      Apply BCs
      Cholesky decomposition
   end if
   P2G mapping, m_αI, v_αI
   Compute particle deformation F_p and effective PK1 stress P'_p
   Compute intermediate accelerations, a*_αI
   Compute pore pressure increment, Δp_I^{t+1}
   Compute update accelerations, a**_αI
   Update particle velocity v_αp, position x_p, and pressure p_p
   t = t + Δt
end while
```

Similarly, the pore pressure for material points can be updated by mapping the incremental nodal pore-pressure value as:

$$p_p^{t+1} = p_p^t + \sum_{I=1}^{n_n} S_{Ip}(p_I^{t+1} - p_I^t) \tag{87}$$

Since the variation of permeability is already incorporated via Equation (37), an independent update of the permeability is not required, in contrast with some ULMPM implementations.

The overall computational flow for the proposed TLMPM is summarized in Algorithm 1.

5 | Numerical Examples

5.1 | One-Dimensional Consolidation

5.1.1 | Small Deformation Consolidation

To validate the proposed TL formulation, we first consider the classical one-dimensional consolidation problem. As shown in Figure 5, a saturated granular column with a height of 1 m is subjected to a constant surcharge $q = 10$ kPa on the permeable top surface. The lateral boundaries and the bottom are constrained in the normal direction and are impermeable. The column is discretized by 50 elements with an element size of $\Delta h_e = 0.02$ m. The material properties are defined as follows: Soil grain density $\rho_s = 2600$ kg/m^3, pore fluid density $\rho_f = 1000$ kg/m^3, initial porosity $\theta_f = 0.3$, Young's modulus $E = 1 \times 10^7$ Pa, and Poisson's ratio $\nu = 0.25$. For the simulation parameters, we select the flip velocity update scheme, stability parameter $\tau = 0$, and time step $\Delta t = 1 \times 10^{-4}$ s. The initial stress and pore pressure are set to zero, and the gravity is neglected. Under these conditions, the soil column experiences only small deformations without cell-crossing noise, and thus, standard MPM is employed for the simulation. Unless otherwise stated, we use the consistent mass matrix for the TL simulation and the lumped mass matrix for the UL counterpart.

The analytical solution for one-dimensional consolidation is well established in Reference [62]. The evolution of pore pressure $p(y, t)$ is given by:

$$p(y,t) = \frac{4p_0}{\pi} \sum_{M=0}^{\infty} \frac{1}{2M+1} \sin\left(\frac{(2M+1)\pi y}{2H}\right) e^{-(2M+1)^2\pi^2 T_v/4} \tag{88}$$

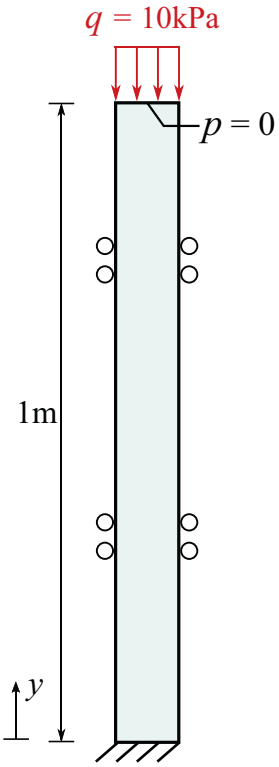

FIGURE 5 | Schematic of the one-dimensional consolidation model.

$$T_v = \frac{k}{\gamma_f m_v}\frac{t}{H^2} \tag{89}$$

where p_0 is the surcharge exerted at the top of the column, H is the column height, and T_v is a dimensionless time factor related to the constrained modulus of the solid phase m_v. The surface settlement $u(t)$ and the degree of consolidation (normalized settlement) U are computed as:

$$u(t) = m_v p_0 H\left(1 - \frac{8}{\pi^2}\sum_{M=0}^{\infty}\frac{1}{(2M+1)^2}e^{-(2M+1)^2\pi^2 T_v/4}\right) \tag{90}$$

$$U = \frac{u(t)}{u(+\infty)} \tag{91}$$

Figure 6 illustrates the evolution of pore pressure and the degree of consolidation over time. Given the relatively high stiffness of the solid skeleton, the column experiences only a small settlement, and thus no particles cross element boundaries during the simulation. As expected, both the TL and UL yield nearly identical results and agree well with the analytical solution, thereby confirming the accuracy of the proposed approach in small deformation scenarios.

In the present study, to investigate whether the TL semi-implicit formulation can provide a larger critical time step compared to the UL formulation [26], we conducted a series of modeling of consolidation. In this problem, the standard MPM shape function is adopted, and the time step is adjusted to determine the critical time step sizes for both formulations under varying permeability conditions. The results are summarized in Figure 7.

Our results show that, as expected, the TL semi-implicit formulation yields a critical time step of the same order as the UL counterpart. While the critical time step size of TL formulation is slightly smaller than that of UL, it shows reduced sensitivity to permeability variations. At high permeability levels, the TL formulation maintains more consistent stability characteristics, without the pronounced reductions observed in the UL formulation. Additionally, both TL and UL semi-implicit formulations allow for significantly larger time steps compared to the explicit MPM, particularly in low-permeability scenarios where the explicit method's time step is severely constrained by permeability effects.

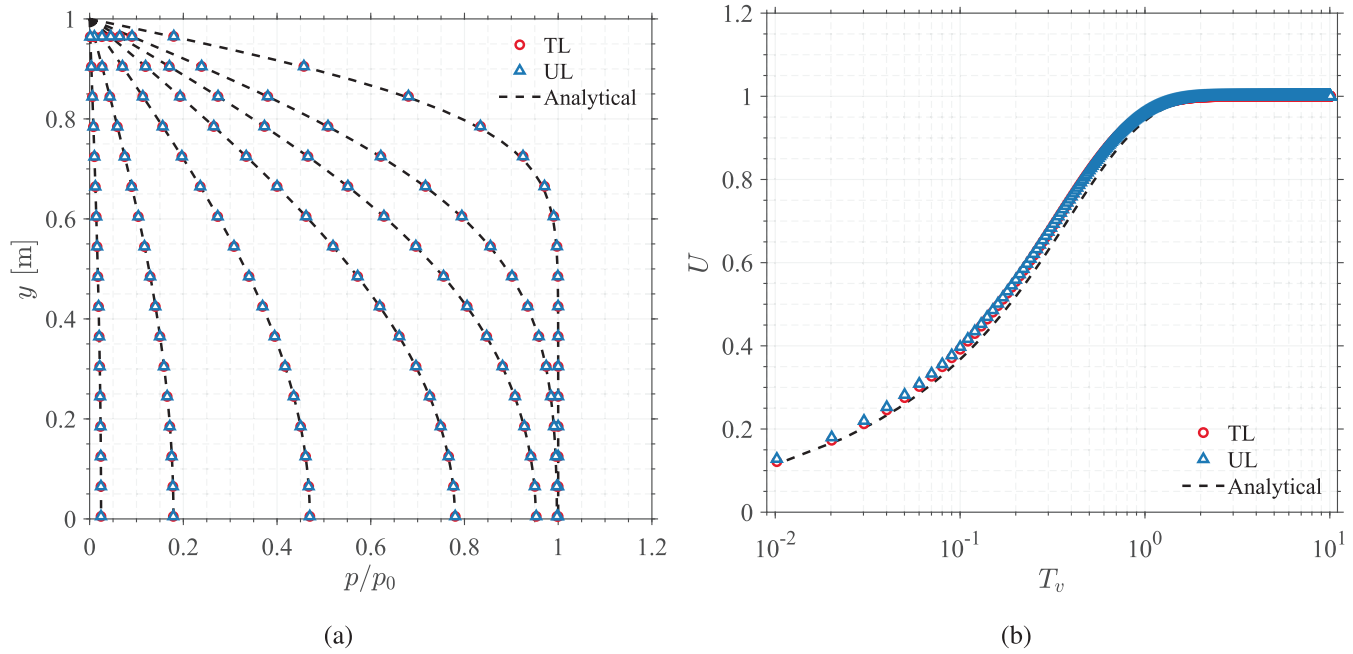

FIGURE 6 | Pore pressure evolution (a) and degree of consolidation (b) for small deformation consolidation.

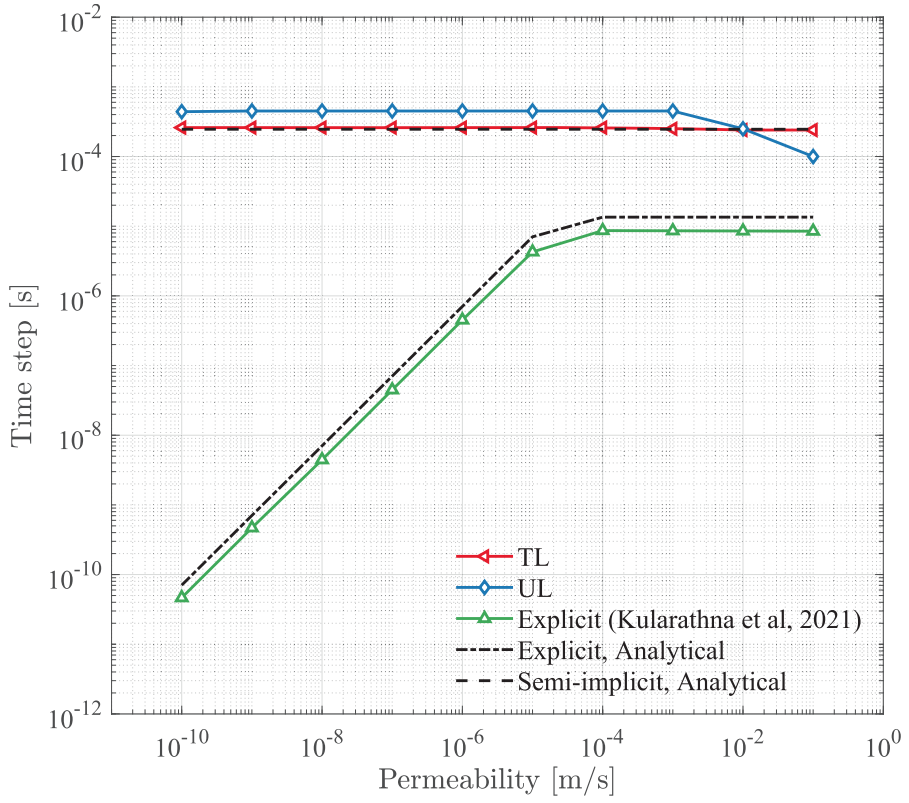

FIGURE 7 | Critical time step size versus permeability for the explicit and semi-implicit MPM.

5.1.2 | Finite Strain Consolidation

To further evaluate the performance of the TL framework under finite strain conditions, Young's modulus is reduced by a factor of ten to $E = 1 \times 10^6$ Pa, while all other material and control parameters remain unchanged from the previous setup. Again, no pressure stabilization techniques are applied in this example. Both MPM and GIMP are employed to simulate the consolidation process using the TL and UL formulations. To accurately assess the inherent numerical stability under different settings, the artificial pore pressure smoothing technique is not applied in this and subsequent cases. Noted that, although analytical solutions for finite strain consolidation are available (e.g., [63]), they are not used here as their permeability-deformation relationship differs from the Kozeny–Carman function Equation (37) adopted in this study. Instead, for consistency and simplicity, we use Terzaghi's classical solution for comparison [62].

Figure 8 presents the evolution of pore pressure over time, while Figure 9 shows snapshots of pore pressure distribution at selected time instances. As observed, the UL-MPM simulation terminates prematurely at approximately $T_v = 0.3$ due to numerical instability caused by material points crossing element boundaries. As pore pressure dissipates and settlement progresses, material points in the upper region of the column, particularly in the second row from the top, begin to cross element boundaries. This crossing induces abrupt changes in effective stress, leading to an erroneous pore pressure field. Prior to termination, however, the pore pressure evolution in UL-MPM remains stable and agrees well with the analytical solution. In contrast, the UL-GIMP formulation successfully completes the simulation but still exhibits pore pressure instabilities under finite deformation conditions. While GIMP effectively reduces cell-crossing noise in purely solid mechanics problems, it appears insufficient to fully prevent instability in coupled solid-fluid simulations by FSM without additional stabilization techniques, such as pore pressure smoothing or mixed-order interpolation. On the other hand, the TL-based simulations demonstrate superior numerical stability and produce results that closely match the analytical solution. This numerical robustness arises from a fundamental property of the TL formulation that shape functions and their gradients are evaluated at the particles' initial reference positions. Consequently, the downward motion, regardless of particle cell crossing, primarily updates the particles' deformation gradients and the entries of the system matrices. As the mapping between particles and nodes remains unchanged, this behavior in essence mirrors the small-deformation

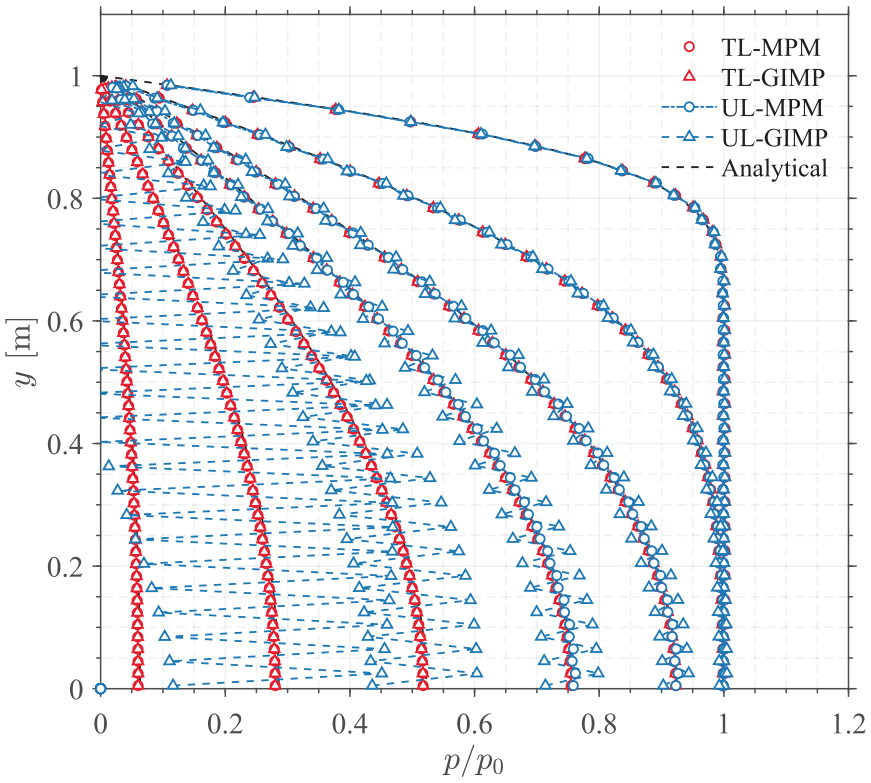

FIGURE 8 | Pore pressure distribution at $T = 0.01$, 0.04, 0.12, 0.21, 0.36, and 0.61. Note that some results for UL-MPM and UL-GIMP are not presented due to simulation failure.

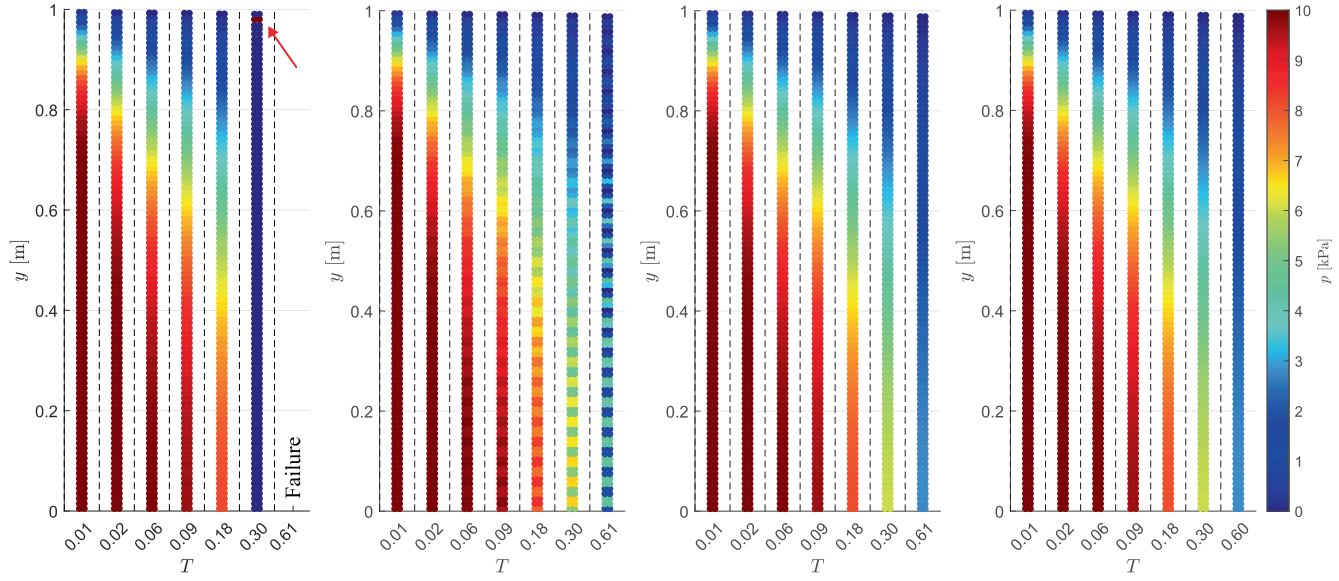

(a) UL-MPM (b) UL-GIMP (c) TL-MPM (d) TL-GIMP

FIGURE 9 | Snapshots of pore pressure distribution for finite strain consolidation at selected dimensionless times, using (a) UL-MPM, (b) UL-GIMP, (c) TL-MPM, and (d) TL-GIMP. The red arrow highlights the initial location of material point cell-crossing and the failure of analysis of the standard UL-MPM.

consolidation case. As a result, the TL-based MPM could achieve a satisfactory result without encountering any stability issues.

5.2 | Mandel's Problem

Next, we consider Mandel's problem, one of the earliest engineering applications of Biot's theory of poroelasticity. This benchmark is intended to address the intricate coupling between solid deformation and pore pressure dissipation in a poroelastic medium.

Figure 10 illustrates the schematic of Mandel's problem. Herein, we consider a rectangular, fully saturated, and isotropic porous medium with a width of $2a$ and a height of $2b$. The specimen is bounded by two rigid, impermeable, and frictionless plates at the top and bottom, while its lateral sides are permeable. At time $t = 0$, a vertical load of $2F$ (force per unit length) is applied to the top and bottom plate, initiating the coupled process of deformation and pore pressure dissipation.

The analytical solutions for the pore pressure and the vertical displacement are given by

$$p(x,t) = 2p_0 \sum_{n=1}^{\infty} \frac{\sin\beta_n}{\beta_n - \sin\beta_n \cos\beta_n} \left(\cos\frac{\beta_n x}{a} - \cos\beta_n\right) \exp\left(-\frac{\beta_n^2 ct}{a^2}\right) \tag{92}$$

$$u_y(y,t) = u_{y,0} + \left(\frac{F(1-\nu_u)}{\mu a} \sum_{n=1}^{\infty} \frac{\sin\beta_n \cos\beta_n}{\beta_n - \sin\beta_n \cos\beta_n} \exp\left(-\frac{\beta_n^2 ct}{a^2}\right)\right) y \tag{93}$$

where the initial pore pressure p_0 and the initial vertical displacement $u_{y,0}$ induced by F are defined as:

$$p_0 = \frac{1}{3a} B(1+\nu_u) F \tag{94}$$

$$u_{y,0} = -\frac{F(1-\nu_u)y}{2\mu a} \tag{95}$$

In above, $B = \alpha M / K_u$ is Skempton's coefficient, α is Biot's coefficient, $M = \left(\frac{\theta_f}{K_f} + \frac{\alpha - \theta_f}{K_s}\right)^{-1}$ is the Biot modulus with K_f and K_s being the bulk moduli of the pore fluid and solid grains, respectively. $\upsilon_u = (3\nu + \alpha B(1-2\nu))/(3 - \alpha B(1 -$

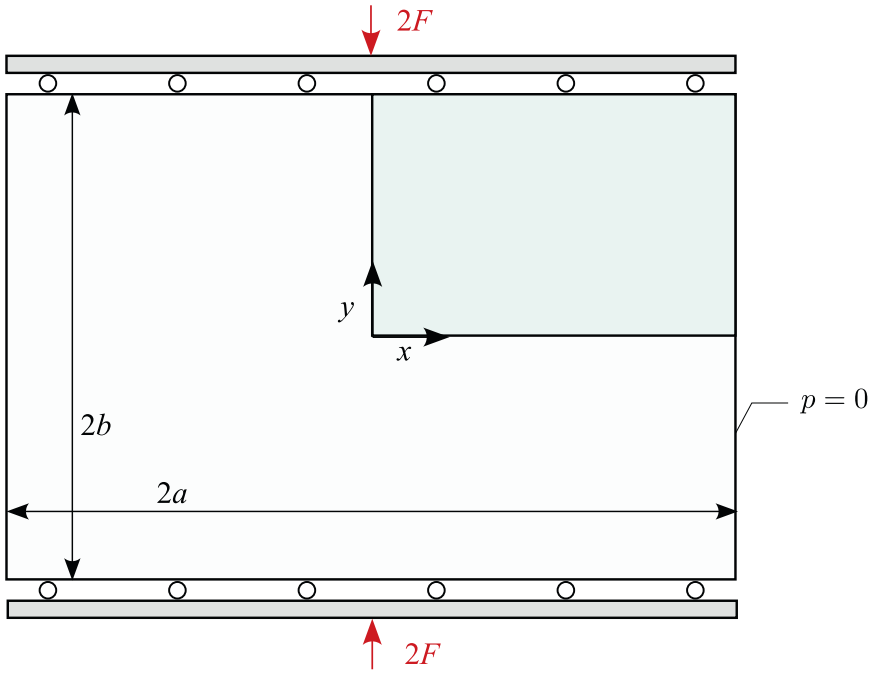

FIGURE 10 | Model setup for the two-dimensional Mandel's problem.

2ν)) is the undrained Poisson's ratio. The consolidation coefficient c is defined as $c = kM/\left(\rho g + \alpha^2 \rho g M c_M\right)$, k is the permeability, $c_M = (\lambda + 2\mu)^{-1}$ is the vertical uniaxial compressibility, $K_u = \lambda + \frac{2}{3}\mu + \alpha^2 M$ is the undrained bulk modulus, where λ and μ are the Lamé coefficients. The parameter β_n is the positive root of the below nonlinear characteristic equation

$$\tan \beta_n = \frac{1-\nu}{\nu_u - \nu}\, \beta_n \tag{96}$$

To exploit symmetry, only a quarter of the domain is modeled in the simulation, with $a = 15$ m and $b = 10$ m. The left and bottom boundaries are constrained in the normal direction and are impermeable. A uniformly distributed vertical load of $F = 15$ kN/m is applied to the top surface, which is impermeable, while the right boundary remains permeable. The domain is discretized by quadrilateral elements with a cell size of $\Delta h_e = 0.5$ m, and each cell contains four material points. The pore pressure stability coefficient is set to $\tau = 1$. The time step is $\Delta t = 1 \times 10^{-4}$ s and the total simulation time is 200 s. The material properties are set as follows: Soil grain density $\rho_s = 2600$ kg/m^3, pore fluid density $\rho_f = 1000$ kg/m^3, initial porosity $\theta_f = 0.3$, Young's modulus $E = 1 \times 10^8$ Pa and Poisson's ratio $\nu = 0.25$. Biot's coefficient α is taken as 1. Under the assumption that both the solid grains and pore fluid are fully incompressible, it follows that $M \to \infty$, $K_u \to \infty$, $B \to 1$, and $\upsilon_u \to 0.5$. Standard MPM is adopted for both ULMPM and TLMPM.

Figure 11 displays the pore pressure and vertical displacement obtained using the TL method at $t = 20$ s. The pore pressure primarily decreases from the left to the right permeable boundary. The vertical settlement on the right side of the domain exhibits slightly larger values due to dissipated pore pressure and higher effective stress. For further validation, six monitoring points are selected along the x-axis ($x = \frac{1}{4}a, \frac{1}{2}a, \frac{3}{4}a$) and y-axis ($y = \frac{1}{4}b, \frac{1}{2}b, \frac{3}{4}b$). As shown in Figure 12a, both the UL and TL simulations align well with the analytical solution and capture both pore pressure dissipation and displacement evolution. A key observation is that, immediately after load application, the pore pressure (particularly at $x = \frac{1}{4}a$) exceeds the initial pressure p_0 before gradually decreasing. This non-monotonic behavior is known as the Mandel–Cryer effect, is an intricate interaction between mechanical deformation and pore fluid dissipation. Upon loading, the sudden compression of the porous medium induces an initial increase in pore pressure. However, due to the viscosity, the fluid takes time to redistribute, resulting in a temporary pressure buildup in regions away from the drainage boundaries. As time progresses, fluid flow towards the permeable boundaries facilitates pressure dissipation, causing the excess pore pressure to decline.

As discussed in Section 4.2, the TL framework employs an update interval n_k for regularly update the coefficient matrix $\boldsymbol{\mathcal{A}}^t$, which may influence both computational speed and simulation accuracy. To evaluate the effect of n_k, we performed a series of simulations with different n_k. Figure 13 shows the normalized pore pressure discrepancy $\Delta p/p_0 = (p_{\text{sim}} - p_{\text{ana}})/p_0$

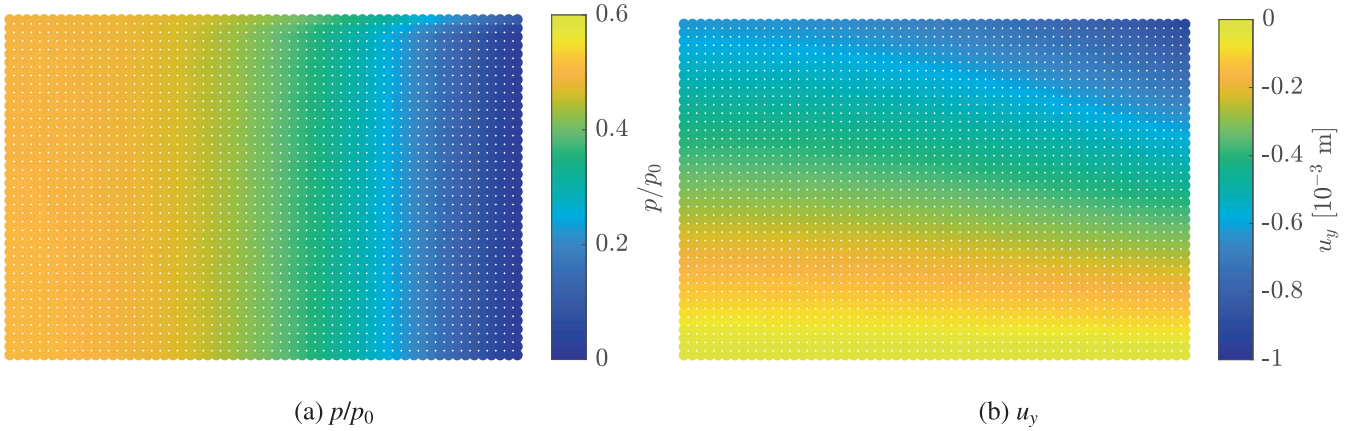

(a) p/p_0 (b) u_y

FIGURE 11 | Normalized pore pressure p/p_0 and vertical displacement u_y by TL-MPM at $t = 20$ s. (a) p/p_0, (b) u_y.

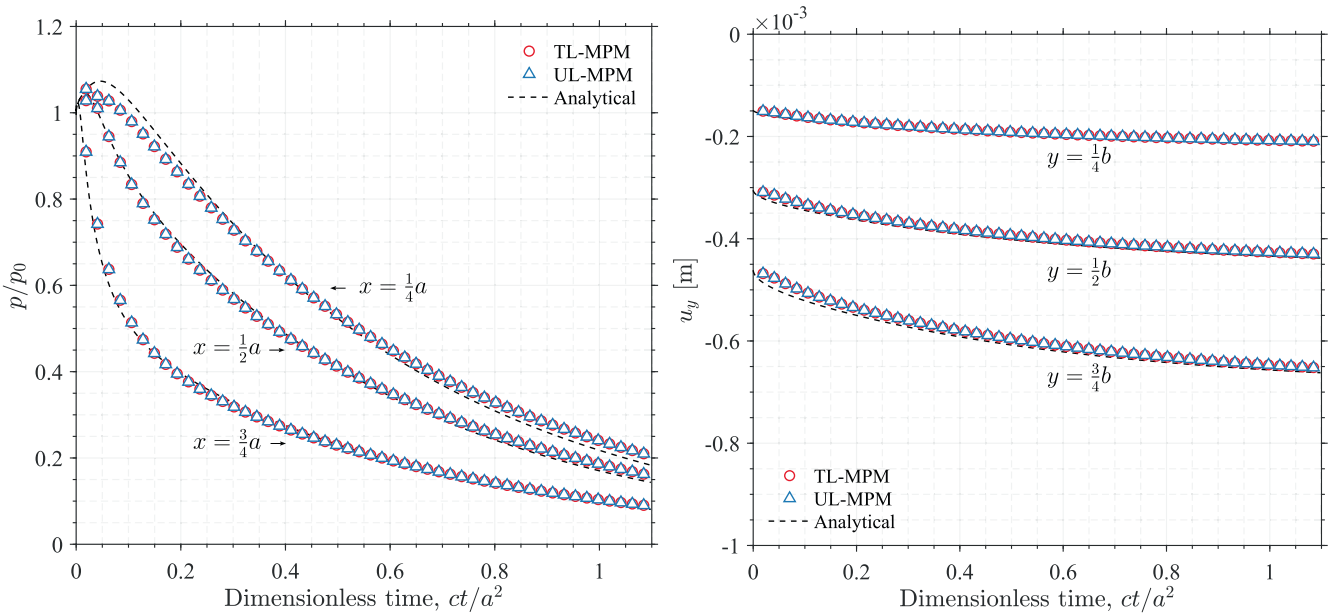

(a) Pore pressure evolution at monitor points at x-axis. (b) Vertical displacement evolution at monitor points at y-axis.

FIGURE 12 | Pore pressure evolution and settlement for monitor particles. (a) Pore pressure evolution at monitor points at x-axis, (b) Vertical displacement evolution at monitor points at y-axis.

at the point $\left(\frac{1}{2}a, 0\right)$ for various n_k values, while Figure 14 presents the runtime for each simulation scenario. For reference, results obtained using the UL method, which has a runtime of 138, 200 s, are also included. At the onset of loading, significant oscillations in pore pressure are observed due to the sudden application of the external force F. In the FSM, the effective stress is treated explicitly, whereas pore pressure is handled implicitly, leading to a delay in re-balancing the external load and resulting in these oscillations. After that, the influence of n_k on pore pressure error is quite minimal, at least for the consolidation problem. Remarkably, even when $n_k = 1$, where no matrix factorization or decomposition is performed, the TL method remains significantly faster than the UL method, with a runtime of 43, 550 s, achieving approximately 3.17 speedup compared to UL. This advantage is attributed to the avoidance of computing shape functions, identifying free surface nodes, and reusing intermediate variables, as previously mentioned. Furthermore, as n_k increases, the computational efficiency of TL continues to improve, achieving a speedup of nearly 40.7×. However, increasing n_k beyond 100 does not yield substantial additional speedup, as the overall computational cost becomes dominated by other steps of the MPM, such as G2P and P2G mapping, rather than by solving the linear matrix system. Based on our experience, the appropriate selection of n_k depends on the nature of the problem being solved. In most cases, choosing n_k in the range of 5 to 100 provides a good balance between accuracy and performance. For dynamic and transient problems involving large deformations, where rapid changes of deformation gradient may occur, it is better to use a smaller n_k to

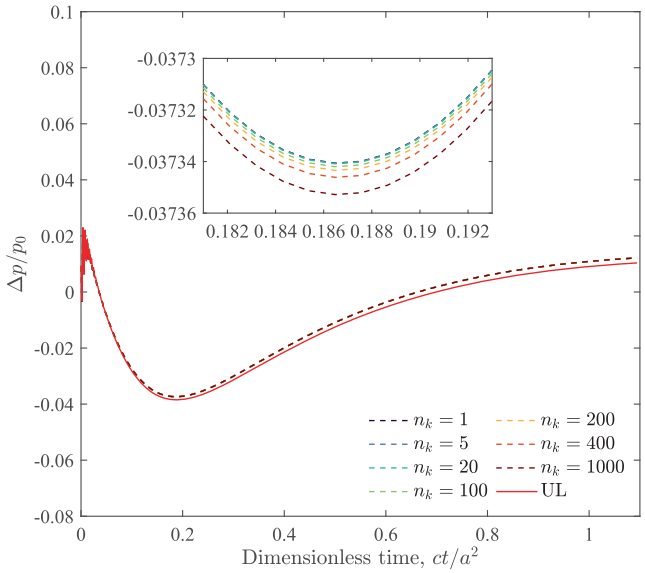

FIGURE 13 | The influence of update interval on the pore pressure error.

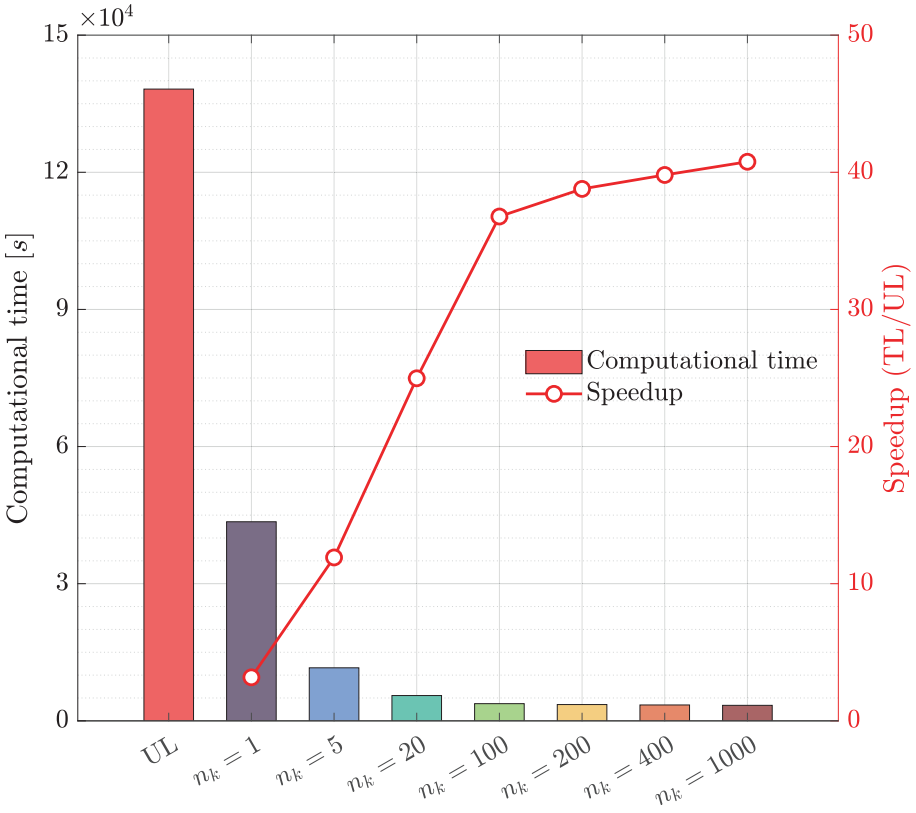

FIGURE 14 | The influence of update interval on the computational time and corresponding speedup.

ensure frequent updates of the coefficient matrix to maintain accuracy. Conversely, for quasi-static problems, a larger n_k is preferable to maximize computational efficiency without sacrificing accuracy.

5.3 | Wave Propagation

We now consider a dynamic problem involving wave propagation in an isotropic, saturated soil domain subjected to an impulsive load. This problem has been widely studied by various numerical methods (e.g., [10, 29, 64–66]). The model

setting is depicted in Figure 15. The saturated soil domain is 21 m in width and 10 m in height, and is discretized into 3360 quadrilateral elements with an element size of $\Delta h_e = 0.25$ m, with each containing four material points. The lateral and the bottom boundaries are constrained in their normal directions and set to be impermeable, while the top surface is permeable. The time step is $\Delta t = 1 \times 10^{-3}$ s and the total simulation time is 0.2 s. The material properties are set as follows: Soil grain density $\rho_s = 2600$ kg/m^3, pore fluid density $\rho_f = 1000$ kg/m^3, initial porosity $\theta_f = 0.3$, Young's modulus $E = 1 \times 10^8$ Pa, and Poisson's ratio $\nu = 0.25$. The permeability k is set as 1×10^{-2} m/s.

To trigger the wave, an impulsive load (in kPa) is applied at the center of the top surface ($x \in [10, 11]$) and is defined by

$$f(t) = 100 \sin(25\pi t)[1 - H(t - 0.04)] + 100 \tag{97}$$

where $H(\circ)$ is the Heaviside step function. As denoted in Figure 15, two monitoring points located at the domain surface, Point A at (5, 10) and Point B at (10.5, 10), are selected to record the local response during wave propagation.

Figure 16a shows the trajectory of Point A. For comparison, solutions from FEM [10] and smoothed particle finite element method (SPFEM) [65] are provided. It is clearly observed that various MPM simulations are capable of capturing the key

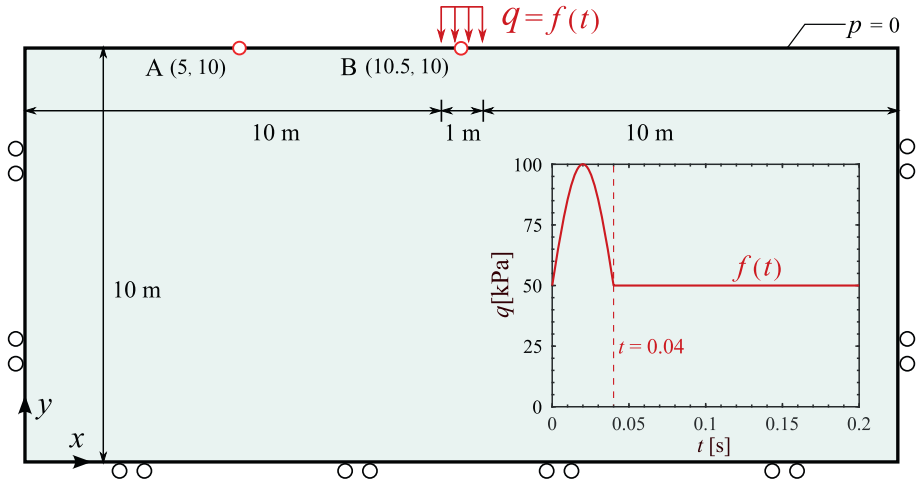

FIGURE 15 | Model setting for wave propagation.

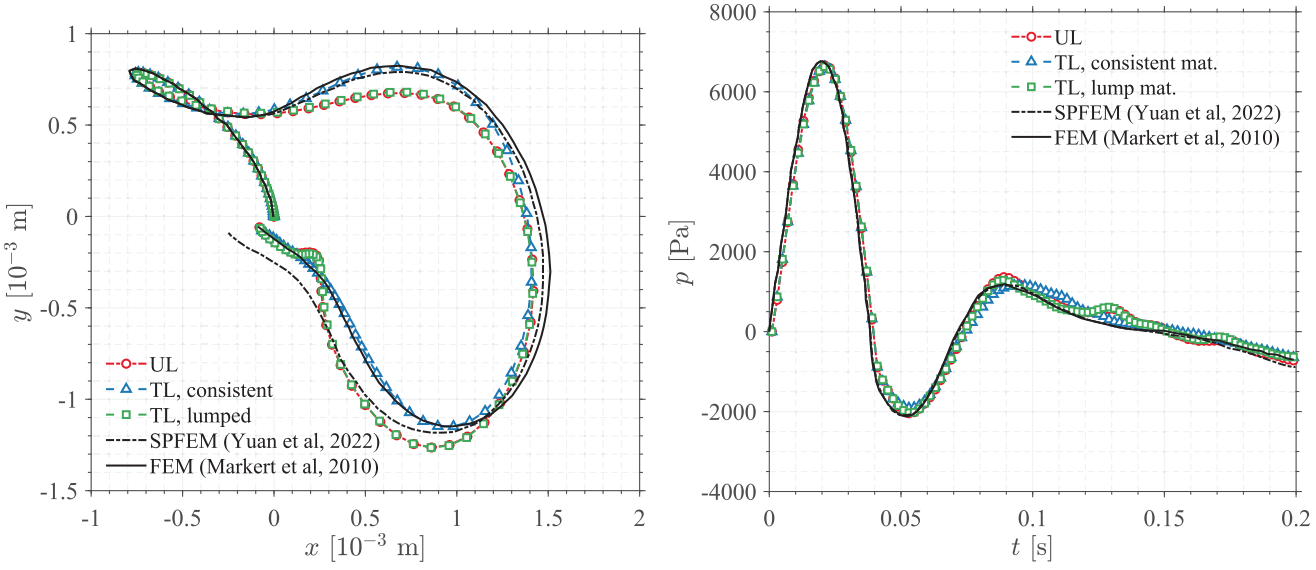

FIGURE 16 | Trajectory for surface material point A (5, 10) and pore pressure evolution for material point C (8, 8).

characteristics of the Rayleigh wave pattern at Point A. However, the UL-MPM and TL-MPM with a lumped mass matrix tend to underestimate the rebound amplitude, resulting in trajectories that are shifted slightly downward relative to the reference solution. These results are generally in agreement with the SPFEM result [65]. In contrast, TL-MPM with a consistent mass matrix yields a more accurate prediction of the wave dynamics, although a slight discrepancy in the lateral wave propagation remains when compared to FEM results [10]. This discrepancy is primarily attributed to mesh resolution effects, which are discussed further below. In terms of pore pressure, the various MPM approaches produce distributions that closely align with the reference models.

To assess the mesh sensitivity for the TL-MPM with a consistent mass matrix, we further conduct the simulation with three mesh resolutions: Coarse ($\Delta h_e = 0.25$ m), medium ($\Delta h_e = 0.20$ m), and fine ($\Delta h_e = 0.125$ m). Figure 17 presents the results from this mesh sensitivity analysis at the monitoring points. As the mesh is refined, the MPM solution progressively converges toward the reference solution.

Figures 18 and 19 present snapshots of the pore pressure field obtained using the TLMPM with lumped and consistent mass matrices, respectively, while Figure 20 shows the difference in pore pressure Δp. Both methods successfully capture the initiation and outward propagation of the pressure wave induced by the impulsive load. At the wavefront, both approaches exhibit relatively smooth pressure variations. However, notable differences emerge in the wake of the propagating wave. For the lumped mass matrix, pronounced oscillations are observed near the free surface, particularly at $t = 0.1$ s and $t = 0.15$ s. These oscillations are likely because the lumped mass matrix redistributes the off-diagonal components, decouples the degrees of freedom, and inevitably introduces artificial high-frequency modes, leading to numerical instability and spurious oscillations. This phenomenon has also been reported in Reference [67]. In contrast, the case with the consistent mass matrix provides a more stable and smoother propagation of pore pressure, with significantly reduced oscillations. The pressure distribution appears more consistent and physically reasonable, suggesting a better preservation of the underlying physics of the system. This comparison highlights a fundamental trade-off between the two mass matrix formulations: While the lumped mass matrix may offer computational efficiency by reducing the cost of solving a linear system, it introduces numerical instability and oscillations that can compromise solution accuracy.

5.4 | Self-Weight Slumping

In the final example, we examine the self-weight slumping problem to assess the performance of the proposed method in the large deformation regime. This benchmark test has also been studied by [60, 68–69]. The problem settings are illustrated in Figure 21.

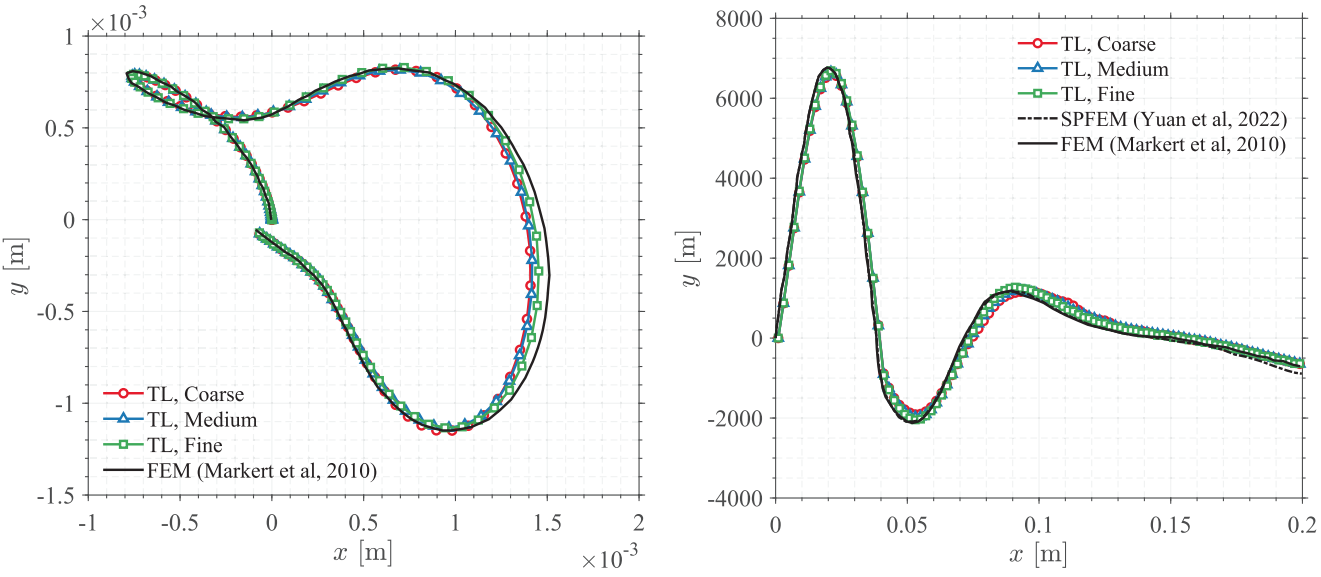

FIGURE 17 | Mesh sensitivity analysis, coarse: $\Delta h_e = 0.25m$, medium: $\Delta h_e = 0.20m$, and fine: $\Delta h_e = 0.125$ m.

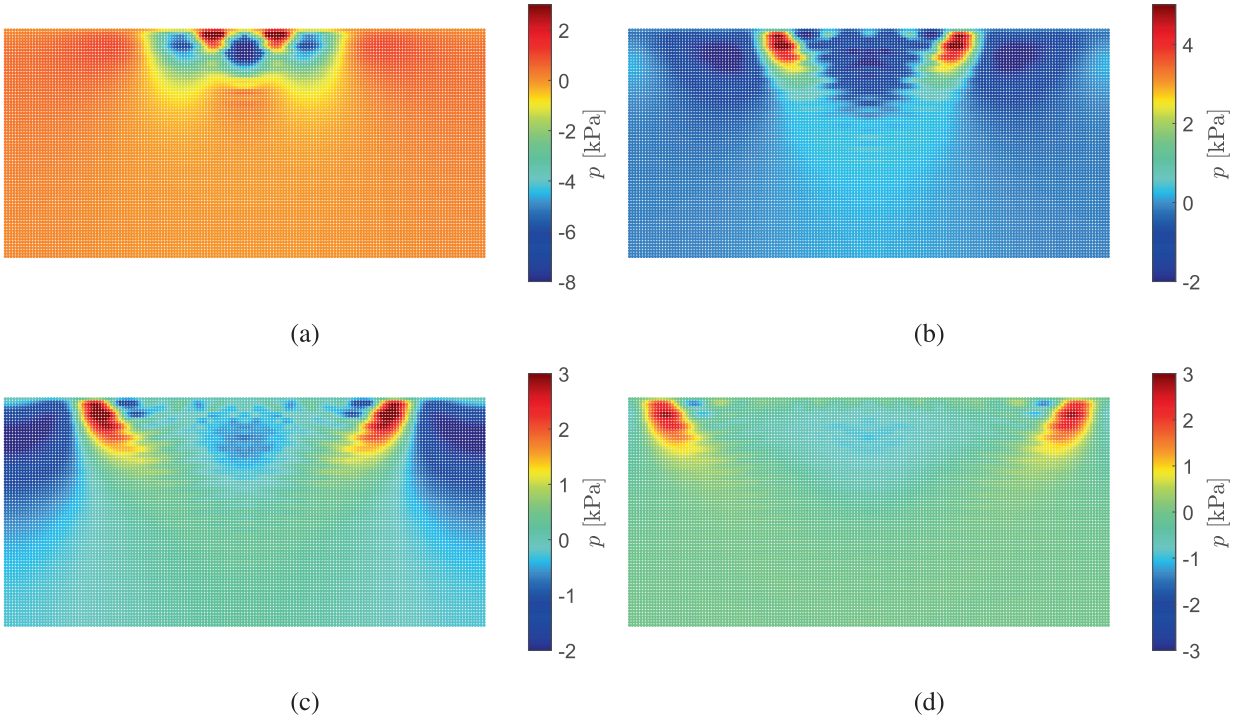

FIGURE 18 | Pore water pressure evolution for TLMPM with lumped mass matrix: (a) $t = 0.05$ s, (b) $t = 0.10$ s, (c) $t = 0.15$ s, and (d) $t = 0.20$ s.

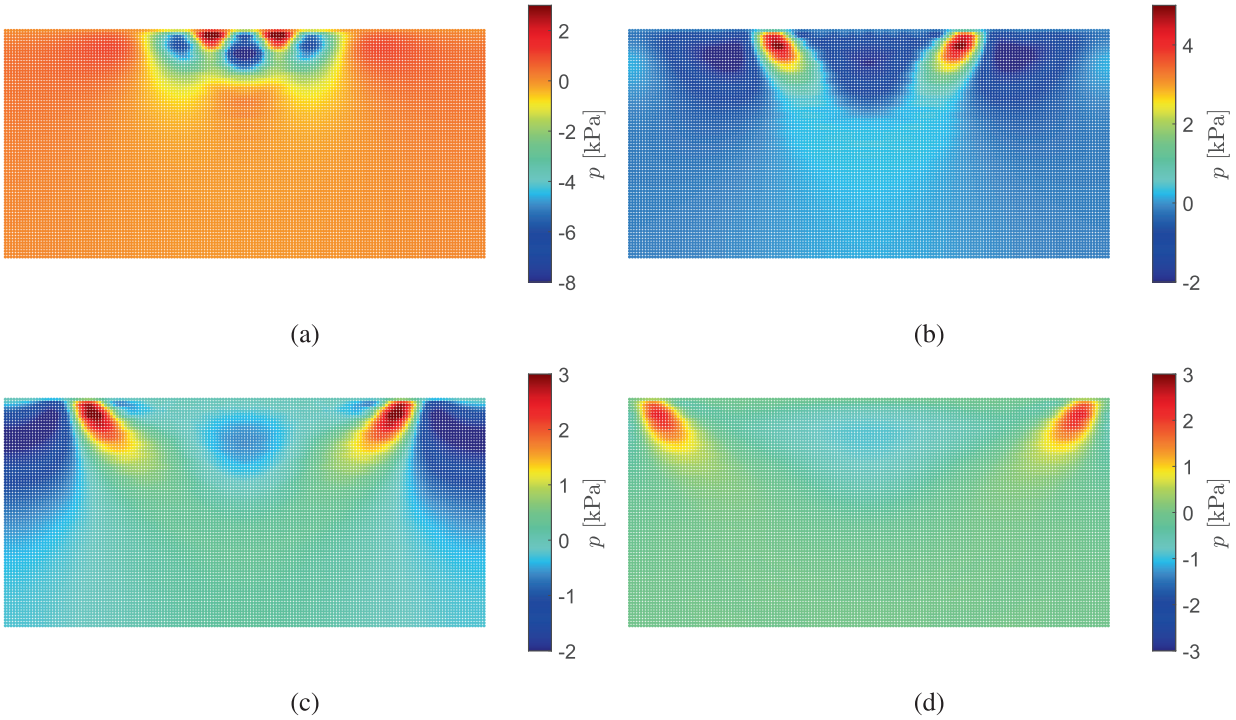

FIGURE 19 | Pore water pressure evolution for TLMPM with consistent mass matrix: (a) $t = 0.05$ s, (b) $t = 0.10$ s, (c) $t = 0.15$ s, and (d) $t = 0.20$ s.

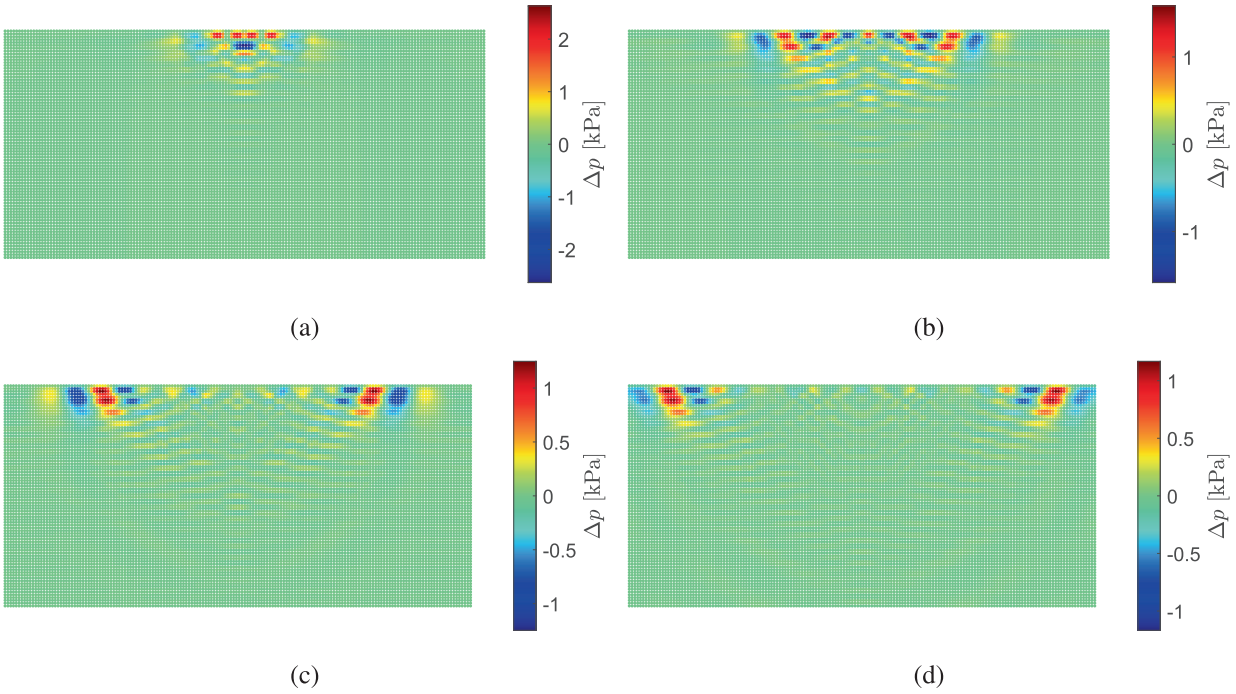

FIGURE 20 | Pore pressure difference between TLMPM with lump mass matrix and consistent mass matrix, where $\Delta p = p_{lump} - p_{consistent}$, (a) $t = 0.05$ s, (b) $t = 0.10$ s, (c) $t = 0.15$ s, and (d) $t = 0.20$ s.

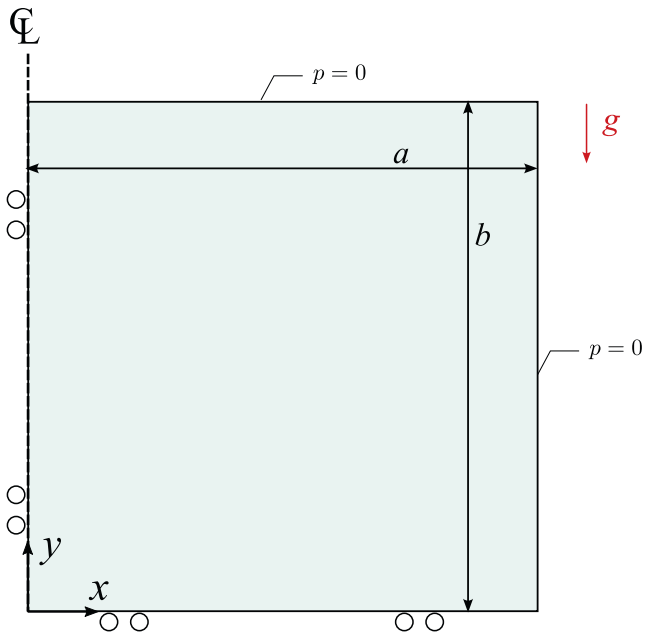

FIGURE 21 | Model setting for self-weight slumping test.

The problem involves a fully saturated elastic block with a width of $2a = 4$ m and a height of $b = 2$ m. By exploiting the symmetry, only the right half of the block is modeled. The bottom and left boundaries are constrained in the normal direction and are impermeable, whereas the top and right boundaries are permeable. The computational domain is discretized by quadrilateral elements with an element size of $\Delta h_e = 0.125$ m. Each cell contains four material points. The slumping is driven by the self-weight of the porous medium. To mitigate severe rebounding of the block, the gravity is ramped linearly to 10 m/s^2 over a period of 0.1 s. Material properties are chosen to be consistent with [68]: Young's modulus for the solid phase $E = 100$ kPa, Poisson's ratio $\nu = 0.3$, density for soil grain $\rho_s = 2650$ kg/m^3, density for the pore fluid $\rho_f = 1000$ kg/m^3, the porosity $\theta_f = 0.4$, and the permeability $k = 1.0 \times 10^{-4}$ m/s. The time step for the simulation

is set to $\Delta t = 2 \times 10^{-3}$ s and the pore pressure stabilization coefficient is defined as $\tau = 1$ for both UL- and TL-MPM. Both standard MPM and GIMP methods are adopted, and again consistent mass matrix is applied in the TL-based simulations.

Figure 22 shows the contour of the displacement field at the final state $t = 0.5$ s. All methods generally reproduce the deformation pattern of the slumping block. However, upon closer examination, UL-MPM results exhibit minor instability and a lack of smoothness, with material points not mobilized uniformly. Instead of displaying a homogeneous deformation, the UL-MPM case shows a staggered distribution of material points, indicating localized numerical errors and fluctuations. This phenomenon is primarily attributed to cell-crossing noise in the effective stress and pore pressure, which is discussed in detail later.

Figure 23 shows the evolution of pore water pressure at different time instances ($t = 0.1$ s, 0.3 s, 0.5 s). As indicated, the UL-MPM result exhibits significant fluctuations and instability. Initially, fluctuations in pore pressure appear only in the center of the domain; however, as the simulation progresses, these instabilities spread throughout the entire domain, leading to strong oscillations and erroneous predictions. This instability arises primarily from cell-crossing effects, which induce sudden changes in effective stress and subsequently alter the pore pressure distribution. Using a higher-order shape function, UL-GIMP offers improved stability, as expected. However, minor unphysical pore pressure values are observed in the lower right corner of the domain. This issue is likely caused by inaccuracies in detecting free surface nodes as deformation progresses, as illustrated in Figure 24, which shows the active free surface nodes for all simulations. In contrast, TL-MPM and TL-GIMP produce almost identical results, both yielding stable and physically consistent pore pressure distributions. This is because the TL formulation focuses on the reference configuration, which inherently avoids cell-crossing noise and ensures that free surface particles/nodes are well-defined and remain unchanged throughout the computation. As a result, the TL approach facilitates accurate pressure evolution and effectively mitigates numerical artifacts.

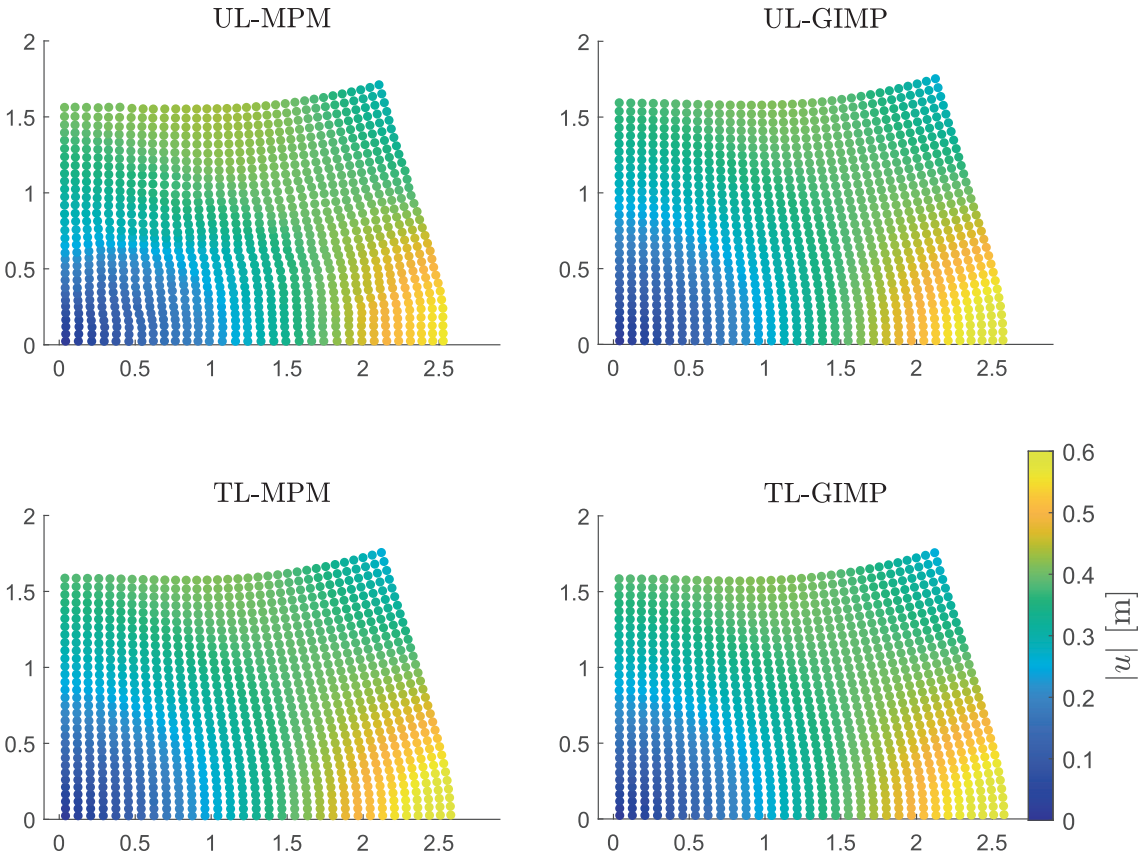

FIGURE 22 | Contour of displacement field at $t = 0.5$ s.

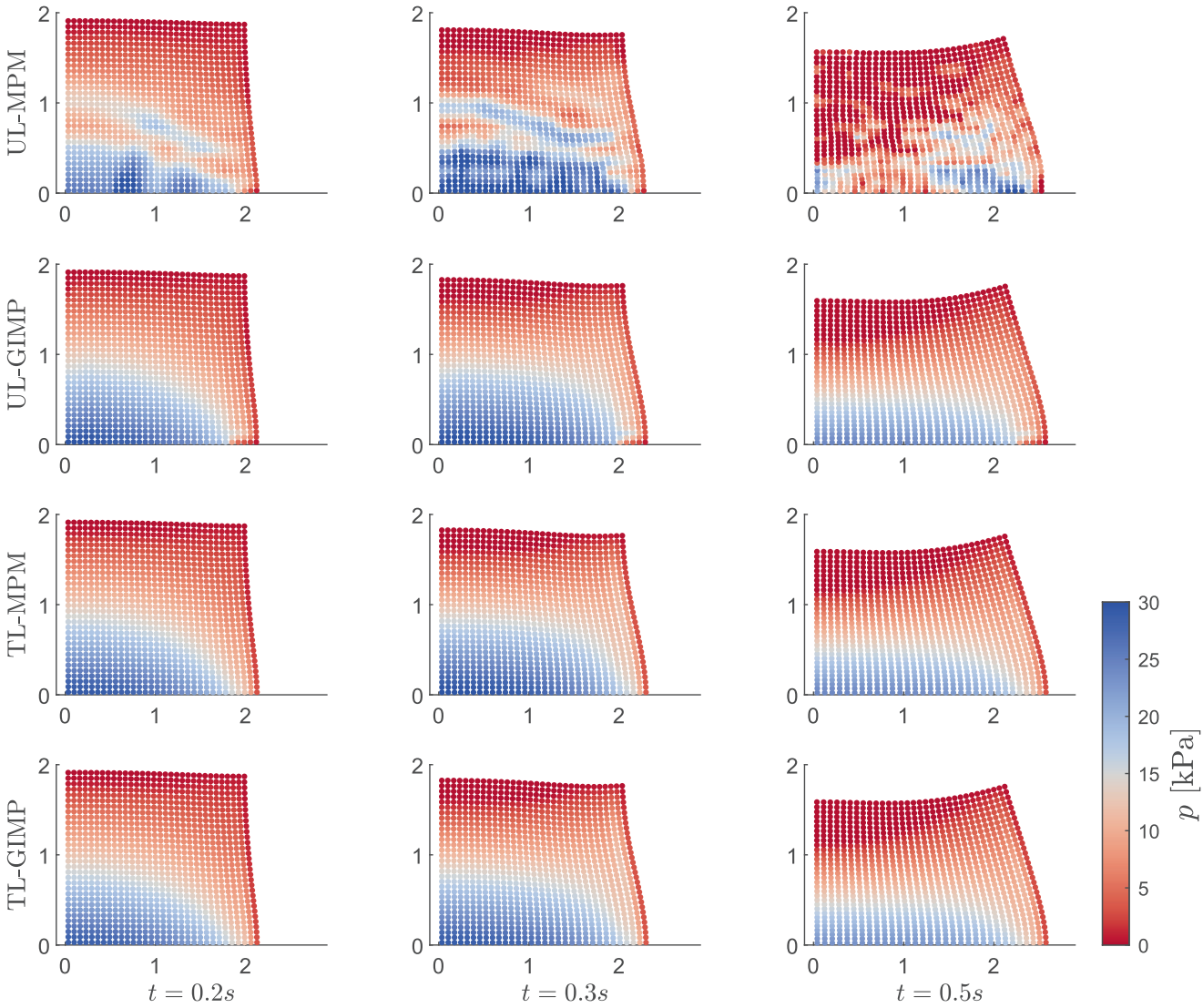

FIGURE 23 | Contour of pore water pressure at $t = 0.1$ s, $t = 0.3$ s, and $t = 0.5$ s.

6 | Discussion

6.1 | Computational Efficiency

Computational efficiency is one of the core advantages of the proposed TLMPM. Table 1 summarizes the runtimes for the numerical examples in this study. Note that the computational time is measured in average runtime per step. This value accounts for all involved computational processes (including the numerical factorization) as it is obtained by dividing the total elapsed time for the whole simulation by the number of steps. The results demonstrate that the TL-based methods significantly outperform the UL counterpart across all cases, with a speedup factor reaching up to 63.82 for the wave propagation simulation. This remarkable performance stems from the fact that the TL method operates in the undeformed reference configuration. Unlike UL-based methods, which require repeated locating of the material point (in which cell) and computing shape functions at every step, TL-based methods compute these quantities once in the reference configuration. Consequently, the active degrees of freedom remain constant, thereby streamlining the assembly of system matrices (see Section 4.2) and reducing the overhead associated with updating shape functions, gradients, and related variables. The TLMPM also obviates the need for real-time detection of free-surface nodes to impose pressure boundary conditions for solving the Poisson equation (see Figure 24). Furthermore, the invariance of the coefficient matrix over certain time intervals permits the use of Cholesky factorization, resulting in significant computational acceleration.

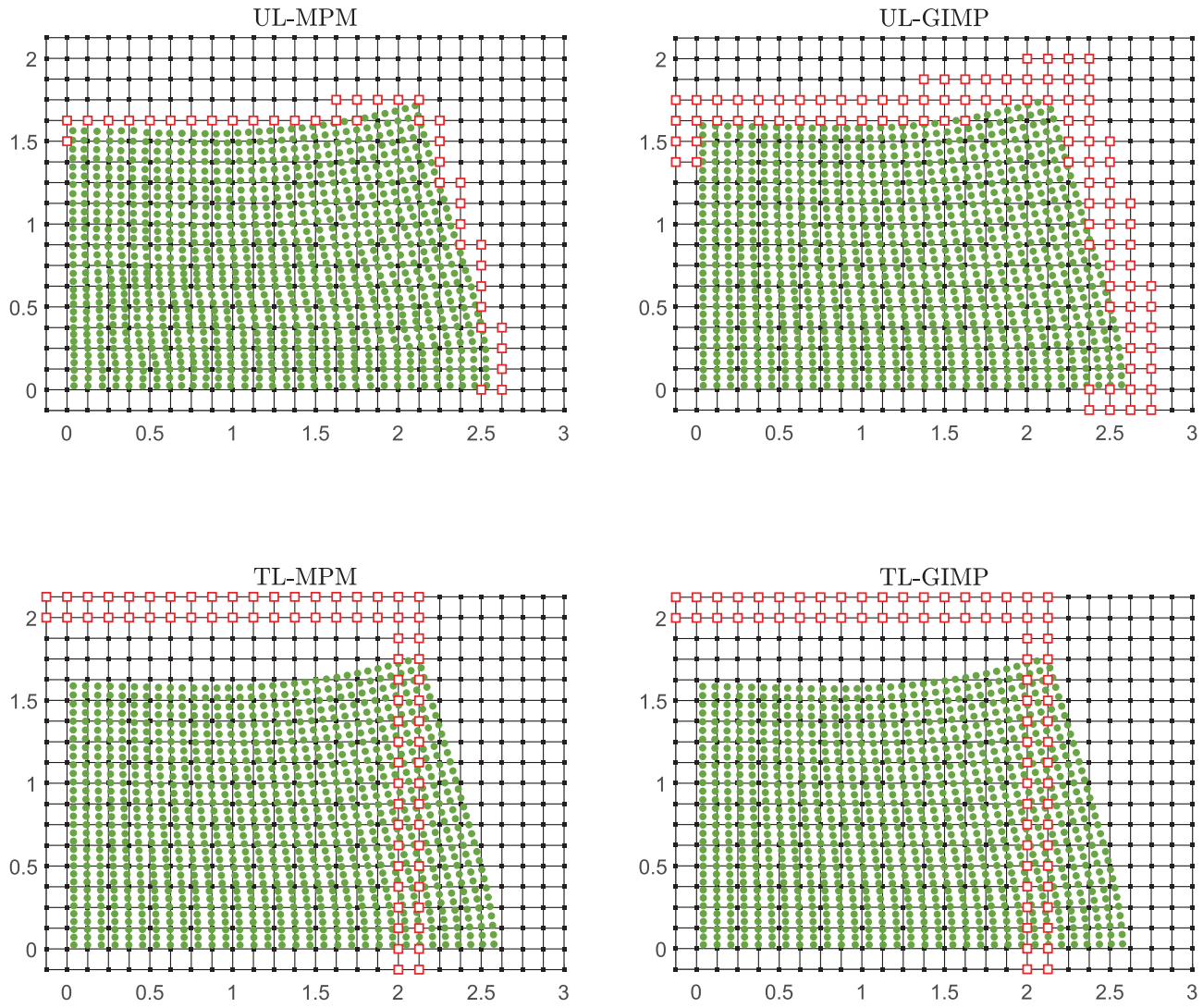

FIGURE 24 | Active free surface node at $t = 0.5$ s.

TABLE 1 | Elapsed time for varying numerical examples.

Example	Section	Particles	Shape func.	n_k [a]	UL [b]	TL [b]	Speedup
1D consolidation	5.1	200	MPM	200	1.43	0.38	3.79
Mandel's problem	5.2	2640	MPM	200	69.10	1.78	38.82
Wave propagation[c]	5.3	13,440	MPM	200	2740.00	42.94	63.82
Slumping	5.4	1024	MPM	5	14.55	1.24	11.73
Slumping	5.4	1024	GIMP	5	40.00	2.10	19.05

[a] For TL only.
[b] Computational time measured at runtime per step [ms/step].
[c] For the coarse mesh case, $\Delta h_e = 0.25$ m.

From the conducted numerical examples, it is observed that the efficiency improvement is more pronounced in larger-scale problems, as evidenced by the higher speedup in the wave propagation case compared to the simpler 1D consolidation example. In the slumping cases, TL-GIMP demonstrates a higher speedup than TL-MPM despite the same number of particles. This difference is attributed to the broader support domains of the GIMP shape functions, which lead to a larger number of degrees of freedom in the assembled system, as well as additional computational overhead associated with detecting active free surface nodes. This finding also highlights the significant potential of TL-MPM in more challenging 3D simulations, where computational costs for matrix assembly, free-surface detection, and matrix solving become more substantial. Future work aims to investigate the performance of TL-MPM in 3D cases.

6.2 | Limitation and Future Pathway

Although the proposed TLMPM demonstrates remarkable performance in the hydromechanical analysis of saturated media, it still has some limitations in other unaddressed scenarios. The first limitation involves poroelastoplasticity and the associated strain localization. In the current study, we focus primarily on poroelasticity, where the material topology and particle connectivity are preserved. This assumption allows the method to operate based on the reference configuration. For scenarios such as the formation of compaction bands [70], this framework remains applicable, as particle connectivity is typically maintained despite localized deformation. However, in problems involving strain softening and shear band formation [9], the material may undergo significant topological changes. Such changes challenge the assumption of fixed connectivity and can compromise the accuracy of the simulation if not adequately addressed. To capture these complex phenomena, it may be necessary to dynamically monitor material connectivity and adjust the update intervals as well as shape function evaluations. A promising pathway could involve adaptively transitioning from a Total Lagrangian to an Updated Reference Lagrangian formulation, as has been successfully implemented in SPH [71, 72]. Furthermore, transitioning to an Eulerian formulation could also be a viable approach for extreme deformation scenarios [73].

Second, and closely related, modeling new boundaries that emerge under large deformations is non-trivial in TLMPM and requires additional modeling and implementation efforts. This is because kinematics and quadrature are referenced to the initial configuration. Therefore, the formation of interfaces not present in the reference state, the exposure of new outward normals, or contact with previously unoccupied regions are not naturally accommodated. This can lead to boundary condition enforcement errors (e.g., Dirichlet pore pressure boundaries) near newly created boundaries, particularly in cases involving severe shear, tearing, fragmentation, or significant self-contact. Under these circumstances, periodic re-referencing or the aforementioned mixed TL/UL scheme to better track evolving boundaries or activating boundary detection functions, and reconstructing free surfaces could be employed. These numerical treatments are, to some degree, compatible with the current framework and may provide a concrete path to handle emerging boundaries effectively.

Another challenge of TLMPM involves material breakage and fracture processes, such as rock fracture and hydraulic fracturing [74, 75]. However, this limitation arises not from the TL formulation itself but from the inherent constraints of the single-valued displacement field in MPM. To address this issue and enable accurate modeling of fracture mechanics, multiple velocity fields can be incorporated into the implementation [76], or enriched shape functions could be introduced [77]. These advancements would allow for the proper representation of discontinuities and fractures in the proposed TLMPM framework.

7 | Closure

This study introduced and evaluated an efficient and stable TLMPM framework for modeling incompressible fluid flow in deformable porous media, addressing key limitations inherent in conventional Updated Lagrangian formulations. By employing a reference configuration to evaluate shape functions, their gradients, and the associated matrices, the TLMPM effectively circumvents errors associated with changing material-point and background mesh connectivity, while at the same time, eliminating the repetitive computational overhead of updating these quantities at every time step. As a result, the TLMPM demonstrates marked numerical stability and enhanced computational efficiency even under large deformation scenarios. The main conclusions drawn from this study are as follows:

- The TLMPM consistently produces more stable and accurate predictions of both pore pressure evolution and mechanical deformation across a broad range of loading conditions, from small deformations to finite strain regimes, primarily due to its inherent ability to bypass cell-crossing noise and the use of optimally positioned quadrature points.
- For all examined examples, the method exhibits notable insensitivity to the choice of shape function. Results obtained using standard MPM formulations are nearly identical to those acquired with higher-order shape functions, implying significant potential for accurate and efficient analysis of large-scale systems.
- In the context of dynamic phenomena, the TLMPM achieves superior performance, particularly when a consistent mass matrix formulation is employed. In comparison, the use of a lumped mass matrix may discard inter-node interactions and introduce high-frequency oscillations.
- The TLMPM offers substantial computational speedups (e.g., up to 63×) compared to conventional Updated Lagrangian formulations, with efficiency gains becoming more pronounced for larger problems. This advantage

arises from the strategic use of the undeformed reference configuration, which permits the use of numerical factorization and obviates the need for real-time detection of free-surface particles when enforcing boundary conditions in the Poisson equation. This feature also highlights the immense potential of the TLMPM for tackling large, computationally intensive problems in geomechanics and related fields, like 3D problems.

Author Contributions

Weijian Liang: conceptualization, methodology, implementation, validation, formal analysis, visualization, writing – original draft. **Bodhinanda Chandra:** methodology, validation, investigation, formal analysis, writing – original draft. **Jidu Yu:** investigation, validation, writing – review and editing. **Zhen-Yu Yin:** resources, supervision, writing – review and editing. **Jidong Zhao:** resources, supervision, writing – review and editing.

Acknowledgments

This research is financially supported by the Research Grants Council (RGC) of Hong Kong (by GRF Project Grant No. 15229223, 15232224 and TRS Project Grant No. T22-607/24N) and National Science Foundation of China (by Grant No. 52508394).

Conflicts of Interest

The authors declare no conflicts of interest.

Data Availability Statement

The data that support the findings of this study are available from the corresponding author upon reasonable request. Data will be made available on request.

Endnotes

[1] While it is true that conformity of the boundary conditions cannot always be guaranteed—that is, when the material boundary becomes nonconforming to the element boundary—the problems simulated in many MPM works still benefit significantly from using conforming BCs (see [61]).

References

1. F. Ceccato, A. Yerro, and G. Di Carluccio, "Simulating Landslides With the Material Point Method: Best Practices, Potentialities, and Challenges," *Engineering Geology* 338 (2024): 107614, https://doi.org/10.1016/j.enggeo.2024.107614.

2. C. W. W. Ng, Z. Jia, S. Poudyal, A. Bhatta, and H. Liu, "Two-Phase MPM Modelling of Debris Flow Impact Against Dual Rigid Barriers," *Géotechnique* 74, no. 12 (2024): 1390–1403, https://doi.org/10.1680/jgeot.22.00199.

3. Z. Lu, F. Zhu, Y. Higo, and J. Zhao, "Coupled Semi-Lagrangian and Poroelastic Peridynamics for Modeling Hydraulic Fracturing in Porous Media," *Computer Methods in Applied Mechanics and Engineering* 437 (2025): 117794, https://doi.org/10.1016/j.cma.2025.117794.

4. F. Ceccato, L. Beuth, P. A. Vermeer, and P. Simonini, "Two-Phase Material Point Method Applied to the Study of Cone Penetration," *Computers and Geotechnics* 80 (2016): 440–452, https://doi.org/10.1016/j.compgeo.2016.03.003.

5. W. Liang, J. Zhao, H. Wu, and K. Soga, "Multiscale Modeling of Anchor Pullout in Sand," *Journal of Geotechnical and Geoenvironmental Engineering* 147, no. 9 (2021): 04021091, https://doi.org/10.1061/(ASCE)GT.1943-5606.0002599.

6. W. Liang, S. Zhao, H. Wu, and J. Zhao, "Bearing Capacity and Failure of Footing on Anisotropic Soil: A Multiscale Perspective," *Computers and Geotechnics* 137 (2021): 104279, https://doi.org/10.1016/j.compgeo.2021.104279.

7. W. Liang and J. Zhao, "Multiscale Modeling of Large Deformation in Geomechanics," *International Journal for Numerical and Analytical Methods in Geomechanics* 43, no. 5 (2019): 1080–1114, https://doi.org/10.1002/nag.2921.

8. R. I. Borja, "A Finite Element Model for Strain Localization Analysis of Strongly Discontinuous Fields Based on Standard Galerkin Approximation," *Computer Methods in Applied Mechanics and Engineering* 190, no. 11 (2000): 1529–1549, https://doi.org/10.1016/S0045-7825(00)00176-6.

9. J. E. Andrade and R. I. Borja, "Modeling Deformation Banding in Dense and Loose Fluid-Saturated Sands," *Finite Elements in Analysis and Design* 43, no. 5 (2007): 361–383, https://doi.org/10.1016/j.finel.2006.11.012.

10. B. Markert, Y. Heider, and W. Ehlers, "Comparison of Monolithic and Splitting Solution Schemes for Dynamic Porous Media Problems," *International Journal for Numerical Methods in Engineering* 82, no. 11 (2010): 1341–1383, https://doi.org/10.1002/nme.2789.

11. J. Choo and R. I. Borja, "Stabilized Mixed Finite Elements for Deformable Porous Media With Double Porosity," *Computer Methods in Applied Mechanics and Engineering* 293 (2015): 131–154, https://doi.org/10.1016/j.cma.2015.03.023.

12. J. Choo and S. Lee, "Enriched Galerkin Finite Elements for Coupled Poromechanics With Local Mass Conservation," *Computer Methods in Applied Mechanics and Engineering* 341 (2018): 311–332, https://doi.org/10.1016/j.cma.2018.06.022.

13. A. Khayyer, H. Gotoh, and Y. Shimizu, "On Systematic Development of FSI Solvers in the Context of Particle Methods," *Journal of Hydrodynamics* 34, no. 3 (2022): 395–407, https://doi.org/10.1007/s42241-022-0042-3.

14. T. Gotoh, D. Sakoda, A. Khayyer, et al., "An Enhanced Total Lagrangian SPH for Non-Linear and Finite Strain Elastic Structural Dynamics," *Computational Mechanics* 76, no. 1 (2025): 147–179, https://doi.org/10.1007/s00466-024-02592-z.

15. K. Y. He, Y. F. Jin, X. W. Zhou, Z. Y. Yin, and X. Chen, "An Improved MPM Formulation for Free Surface Flow Problems Based on Finite Volume Method," *Computer Methods in Applied Mechanics and Engineering* 446 (2025): 118264, https://doi.org/10.1016/j.cma.2025.118264.

16. H. Fang and Z. Y. Yin, "Lagrangian Hybrid Element Particle Method (LHEPM) for Incompressible Fluid Dynamics," *Journal of Computational Physics* 541 (2025): 114281, https://doi.org/10.1016/j.jcp.2025.114281.

17. W. Liang, H. Fang, Z. Y. Yin, and J. Zhao, "A Mortar Segment-To-Segment Frictional Contact Approach in Material Point Method," *Computer Methods in Applied Mechanics and Engineering* 431 (2024): 117294, https://doi.org/10.1016/j.cma.2024.117294.

18. H. Gotoh, A. Khayyer, and Y. Shimizu, "Entirely Lagrangian Meshfree Computational Methods for Hydroelastic Fluid-Structure Interactions in Ocean Engineering—Reliability, Adaptivity and Generality," *Applied Ocean research* 115 (2021): 102822, https://doi.org/10.1016/j.apor.2021.102822.

19. H. W. Zhang, K. P. Wang, and Z. Chen, "Material Point Method for Dynamic Analysis of Saturated Porous Media Under External Contact/Impact of Solid Bodies," *Computer Methods in Applied Mechanics and Engineering* 198, no. 17 (2009): 1456–1472, https://doi.org/10.1016/j.cma.2008.12.006.

20. S. Bandara and K. Soga, "Coupling of Soil Deformation and Pore Fluid Flow Using Material Point Method," *Computers and Geotechnics* 63 (2015): 199–214, https://doi.org/10.1016/j.compgeo.2014.09.009.

21. S. Bandara, A. Ferrari, and L. Laloui, "Modelling Landslides in Unsaturated Slopes Subjected to Rainfall Infiltration Using Material Point Method," *International Journal for Numerical and Analytical Methods in Geomechanics* 40 (2016): 1358–1380.

22. K. Abe, K. Soga, and S. Bandara, "Material Point Method for Coupled Hydromechanical Problems," *Journal of Geotechnical and Geoenvironmental Engineering* 140, no. 3 (2014): 04013033, https://doi.org/10.1061/(ASCE)GT.1943-5606.0001011.

23. A. Yerro, E. Alonso, and N. Pinyol, "The Material Point Method for Unsaturated Soils," *Géotechnique* 65, no. 3 (2015): 201–217, https://doi.org/10.1680/geot.14.P.163.

24. K. Soga, E. Alonso, A. Yerro, K. Kumar, and S. Bandara, "Trends in Large-Deformation Analysis of Landslide Mass Movements With Particular Emphasis on the Material Point Method," *Géotechnique* 66, no. 3 (2016): 248–273, https://doi.org/10.1680/jgeot.15.LM.005.

25. X. Lei, S. He, A. Abed, X. Chen, Z. Yang, and Y. Wu, "A Generalized Interpolation Material Point Method for Modelling Coupled Thermo-Hydro-Mechanical Problems," *Computer Methods in Applied Mechanics and Engineering* 386 (2021): 114080, https://doi.org/10.1016/j.cma.2021.114080.

26. S. Kularathna, W. Liang, T. Zhao, B. Chandra, J. Zhao, and K. Soga, "A Semi-Implicit Material Point Method Based on Fractional-Step Method for Saturated Soil," *International Journal for Numerical and Analytical Methods in Geomechanics* 45, no. 10 (2021): 1405–1436, https://doi.org/10.1002/nag.3207.

27. I. Jassim, D. Stolle, and P. Vermeer, "Two-Phase Dynamic Analysis by Material Point Method," *International Journal for Numerical and Analytical Methods in Geomechanics* 37, no. 15 (2013): 2502–2522, https://doi.org/10.1002/nag.2146.

28. Y. Yamaguchi, S. Takase, S. Moriguchi, and K. Terada, "Solid–Liquid Coupled Material Point Method for Simulation of Ground Collapse With Fluidization," *Computational Particle Mechanics* 7, no. 2 (2020): 209–223, https://doi.org/10.1007/s40571-019-00249-w.

29. W. Liang, J. Zhao, H. Wu, and K. Soga, "Multiscale, Multiphysics Modeling of Saturated Granular Materials in Large Deformation," *Computer Methods in Applied Mechanics and Engineering* 405 (2023): 115871, https://doi.org/10.1016/j.cma.2022.115871.

30. M. Xie, P. Navas, and S. López-Querol, "A Stabilised Semi-Implicit Double-Point Material Point Method for Soil–Water Coupled Problems," *Computational Particle Mechanics* (2025), https://doi.org/10.1007/s40571-025-01027-7.

31. J. Yu, J. Zhao, W. Liang, and S. Zhao, "A Semi-Implicit Material Point Method for Coupled Thermo-Hydro-Mechanical Simulation of Saturated Porous Media in Large Deformation," *Computer Methods in Applied Mechanics and Engineering* 418 (2024): 116462, https://doi.org/10.1016/j.cma.2023.116462.

32. J. Yu, J. Zhao, S. Zhao, and W. Liang, "Thermo-Hydro-Mechanical Coupled Material Point Method for Modeling Freezing and Thawing of Porous Media," *International Journal for Numerical and Analytical Methods in Geomechanics* 48, no. 13 (2024): 3308–3349, https://doi.org/10.1002/nag.3794.

33. J. Yu, J. Zhao, W. Liang, and S. Zhao, "Multiscale Modeling of Coupled Thermo-Hydro-Mechanical Behavior in Ice-Bonded Granular Media Subject to Freeze-Thaw Cycles," *Computers and Geotechnics* 171 (2024): 106349, https://doi.org/10.1016/j.compgeo.2024.106349.

34. J. Yu, W. Liang, and J. Zhao, "Enhancing Dynamic Modeling of Porous Media With Compressible Fluid: A THM Material Point Method With Improved Fractional Step Formulation," *Computer Methods in Applied Mechanics and Engineering* 444 (2025): 118100, https://doi.org/10.1016/j.cma.2025.118100.

35. J. Yu, J. Zhao, K. Soga, S. Zhao, and W. Liang, "A Fully Coupled THMC-MPM Framework for Modeling Coupled Phase Transition and Large Deformation in Methane Hydrate-bearing Sediment," *Journal of the Mechanics and Physics of Solids* (2025): 106368.

36. B. Chandra, R. Hashimoto, S. Matsumi, K. Kamrin, and K. Soga, "Stabilized Mixed Material Point Method for Incompressible Fluid Flow Analysis," *Computer Methods in Applied Mechanics and Engineering* 419 (2024): 116644, https://doi.org/10.1016/j.cma.2023.116644.

37. B. Chandra, R. Hashimoto, K. Kamrin, and K. Soga, "Mixed Material Point Method Formulation, Stabilization, and Validation for a Unified Analysis of Free-Surface and Seepage Flow," *Journal of Computational Physics* 519 (2024): 113457.

38. D. Sulsky and M. Gong, "Improving the Material-Point Method," in *Innovative Numerical Approaches for Multi-Field and Multi-Scale Problems. 81*, ed. K. Weinberg and A. Pandolfi (Springer International Publishing, 2016), 217–240.

39. M. Steffen, R. M. Kirby, and M. Berzins, "Analysis and Reduction of Quadrature Errors in the Material Point Method (MPM)," *International Journal for Numerical Methods in Engineering* 76, no. 6 (2008): 922–948, https://doi.org/10.1002/nme.2360.

40. W. Liang, K. Y. He, Y. F. Jin, and Z. Y. Yin, "A Gradient-Smoothed Material Point Method for Reducing Cell Crossing Noise in Large Deformation Problems," *Computers and Geotechnics* 169 (2024): 106169, https://doi.org/10.1016/j.compgeo.2024.106169.

41. A. de Vaucorbeil, V. P. Nguyen, and C. R. Hutchinson, "A Total-Lagrangian Material Point Method for Solid Mechanics Problems Involving Large Deformations," *Computer Methods in Applied Mechanics and Engineering* 360 (2020): 112783, https://doi.org/10.1016/j.cma.2019.112783.

42. A. de Vaucorbeil and V. P. Nguyen, "Modelling Contacts With a Total Lagrangian Material Point Method," *Computer Methods in Applied Mechanics and Engineering* 373 (2021): 113503, https://doi.org/10.1016/j.cma.2020.113503.

43. S. Nezamabadi and F. Radjai, "Explicit Total Lagrangian Material Point Method With Implicit Frictional-Contact Model for Soft Granular Materials," *Granular Matter* 26, no. 3 (2024): 67, https://doi.org/10.1007/s10035-024-01438-y.

44. S. Zhou, G. Chen, L. Qian, and J. Ma, "HLFEMP: A Coupled MPM-FEM Method Under a Hybrid Updated and Total Lagrangian Framework," *Applied Mathematical Modelling* 136 (2024): 115644, https://doi.org/10.1016/j.apm.2024.115644.

45. R. M. Telikicherla and G. Moutsanidis, "An Assessment of the Total Lagrangian Material Point Method: Comparison to Conventional MPM, Higher Order Basis, and Treatment of Near-Incompressibility," *Computer Methods in Applied Mechanics and Engineering* 414 (2023): 116135, https://doi.org/10.1016/j.cma.2023.116135.

46. K. Terzaghi, R. B. Peck, and G. Mesri, *Soil Mechanics in Engineering Practice* (John Wiley & Sons, 1996).

47. W. H. Yuan, H. Zheng, X. Zheng, B. Wang, and W. Zhang, "An Improved Semi-Implicit Material Point Method for Simulating Large Deformation Problems in Saturated Geomaterials," *Computers and Geotechnics* 161 (2023): 105614, https://doi.org/10.1016/j.compgeo.2023.105614.

48. D. S. Morikawa and M. Asai, "Soil-Water Strong Coupled ISPH Based on U-w-p Formulation for Large Deformation Problems," *Computers and Geotechnics* 142 (2022): 104570, https://doi.org/10.1016/j.compgeo.2021.104570.

49. S. Kularathna and K. Soga, "Comparison of Two Projection Methods for Modeling Incompressible Flows in MPM," *Journal of Hydrodynamics, Series B* 29, no. 3 (2017): 405–412, https://doi.org/10.1016/S1001-6058(16)60750-3.

50. J. Kozeny, "Über Kapillare Leitung Des Wassers Im Boden," *Sitz. Der Wien* 136 (1927): 271–306.

51. P. C. Carman, "Fluid Flow Through Granular Beds," *Transactions of the Institution of Chemical Engineers and the Chemical Engineer* 15 (1937): 150–166.

52. G. A. Holzapfel, "Nonlinear Solid Mechanics: A Continuum Approach for Engineering Science," *Meccanica* 37, no. 4 (2002): 489–490, https://doi.org/10.1023/A:1020843529530.

53. S. G. Bardenhagen and E. M. Kober, "The Generalized Interpolation Material Point Method," *Computer Modeling in Engineering and Sciences* 5, no. 6 (2004): 477–496.

54. R. Courant, K. Friedrichs, and H. Lewy, "On the Partial Difference Equations of Mathematical Physics," *IBM Journal of Research and Development* 11, no. 2 (1967): 215–234, https://doi.org/10.1147/rd.112.0215.

55. M. M. J. Mieremet, D. F. Stolle, F. Ceccato, and C. Vuik, "Numerical Stability for Modelling of Dynamic Two-Phase Interaction," *International Journal for Numerical and Analytical Methods in Geomechanics* 40, no. 9 (2016): 1284–1294, https://doi.org/10.1002/nag.2483.

56. W. H. Press, *Numerical Recipes 3rd Edition: The Art of Scientific Computing* (Cambridge University Press, 2007).

57. J. L. Guermond and L. Quartapelle, "On Stability and Convergence of Projection Methods Based on Pressure Poisson Equation," *International Journal for Numerical Methods in Fluids* 26, no. 9 (1998): 1039–1053, https://doi.org/10.1002/(SICI)1097-0363(19980515)26:9<1039::AID-FLD675>3.0.CO;2-U.

58. J. Guermond, P. Minev, and J. Shen, "An Overview of Projection Methods for Incompressible Flows," *Computer Methods in Applied Mechanics and Engineering* 195, no. 44–47 (2006): 6011–6045, https://doi.org/10.1016/j.cma.2005.10.010.

59. J. A. White and R. I. Borja, "Stabilized Low-Order Finite Elements for Coupled Solid-Deformation/Fluid-Diffusion and Their Application to Fault Zone Transients," *Computer Methods in Applied Mechanics and Engineering* 197, no. 49 (2008): 4353–4366, https://doi.org/10.1016/j.cma.2008.05.015.

60. Y. Zhao and J. Choo, "Stabilized Material Point Methods for Coupled Large Deformation and Fluid Flow in Porous Materials," *Computer Methods in Applied Mechanics and Engineering* 362 (2020): 112742, https://doi.org/10.1016/j.cma.2019.112742.

61. B. Chandra, V. Singer, T. Teschemacher, R. Wüchner, and A. Larese, "Nonconforming Dirichlet Boundary Conditions in Implicit Material Point Method by Means of Penalty Augmentation," *Acta Geotechnica* 16, no. 8 (2021): 2315–2335, https://doi.org/10.1007/s11440-020-01123-3.

62. K. Terzaghi, *Theoretical Soil Mechanics* (Chapman and Hall, Limited, 1943).

63. K. H. Xie and C. J. Leo, "Analytical Solutions of One-Dimensional Large Strain Consolidation of Saturated and Homogeneous Clays," *Computers and Geotechnics* 31, no. 4 (2004): 301–314, https://doi.org/10.1016/j.compgeo.2004.02.006.

64. L. Monforte, P. Navas, J. M. Carbonell, M. Arroyo, and A. Gens, "Low-Order Stabilized Finite Element for the Full Biot Formulation in Soil Mechanics at Finite Strain," *International Journal for Numerical and Analytical Methods in Geomechanics* 43, no. 7 (2019): 1488–1515, https://doi.org/10.1002/nag.2923.

65. W. H. Yuan, J. X. Zhu, K. Liu, W. Zhang, B. B. Dai, and Y. Wang, "Dynamic Analysis of Large Deformation Problems in Saturated Porous Media by Smoothed Particle Finite Element Method," *Computer Methods in Applied Mechanics and Engineering* 392 (2022): 114724, https://doi.org/10.1016/j.cma.2022.114724.

66. Y. F. Jin and Z. Y. Yin, "Two-Phase PFEM With Stable Nodal Integration for Large Deformation Hydromechanical Coupled Geotechnical Problems," *Computer Methods in Applied Mechanics and Engineering* 392 (2022): 114660, https://doi.org/10.1016/j.cma.2022.114660.

67. E. Love and D. Sulsky, "An Unconditionally Stable, Energy–Momentum Consistent Implementation of the Material-Point Method," *Computer Methods in Applied Mechanics and Engineering* 195, no. 33–36 (2006): 3903–3925, https://doi.org/10.1016/j.cma.2005.06.027.

68. X. Zheng, F. Pisanò, P. J. Vardon, and M. A. Hicks, "An Explicit Stabilised Material Point Method for Coupled Hydromechanical Problems in Two-Phase Porous Media," *Computers and Geotechnics* 135 (2021): 104112, https://doi.org/10.1016/j.compgeo.2021.104112.

69. W. H. Yuan, H. C. Wang, W. Zhang, B. B. Dai, K. Liu, and Y. Wang, "Particle Finite Element Method Implementation for Large Deformation Analysis Using Abaqus," *Acta Geotechnica* 16 (2021): 2449–2462, https://doi.org/10.1007/s11440-020-01124-2.

70. H. Wu, J. Zhao, and N. Guo, "Multiscale Modeling of Compaction Bands in Saturated High-Porosity Sandstones," *Engineering Geology* 261 (2019): 105282, https://doi.org/10.1016/j.enggeo.2019.105282.

71. P. R. R. de Campos, A. J. Gil, C. H. Lee, M. Giacomini, and J. Bonet, "A New Updated Reference Lagrangian Smooth Particle Hydrodynamics Algorithm for Isothermal Elasticity and Elasto-Plasticity," *Computer Methods in Applied Mechanics and Engineering* 392 (2022): 114680, https://doi.org/10.1016/j.cma.2022.114680.

72. D. S. Morikawa and M. Asai, "A Mixed Total Lagrangian-Updated Lagrangian Smoothed Particle Hydrodynamics Method for Geomechanics Simulations With Discontinuities," *Soils and Foundations* 65, no. 2 (2025): 101593, https://doi.org/10.1016/j.sandf.2025.101593.

73. J. Young, F. Teixeira-Dias, A. Azevedo, and F. Mill, "Adaptive Total Lagrangian Eulerian SPH for High-Velocity Impacts," *International Journal of Mechanical Sciences* 192 (2021): 106108, https://doi.org/10.1016/j.ijmecsci.2020.106108.

74. F. Zhu and J. Zhao, "Peridynamic Modelling of Blasting Induced Rock Fractures," *Journal of the Mechanics and Physics of Solids* 153 (2021): 104469, https://doi.org/10.1016/j.jmps.2021.104469.

75. C. Yang, F. Zhu, and J. Zhao, "Coupled Total- and Semi-Lagrangian Peridynamics for Modelling Fluid-Driven Fracturing in Solids," *Computer Methods in Applied Mechanics and Engineering* 419 (2024): 116580, https://doi.org/10.1016/j.cma.2023.116580.

76. S. G. Bardenhagen, J. E. Guilkey, K. M. Roessig, J. U. Brackbill, W. M. Witzel, and J. C. Foster, "An Improved Contact Algorithm for the Material Point Method and Application to Stress Propagation in Granular Material," *Computer Modeling in Engineering and Sciences* 2, no. 4 (2001): 509–522, https://doi.org/10.3970/cmes.2001.002.509.

77. Y. Liang, B. Chandra, and K. Soga, "Shear Band Evolution and Post-Failure Simulation by the Extended Material Point Method (XMPM) With Localization Detection and Frictional Self-Contact," *Computer Methods in Applied Mechanics and Engineering* 390 (2022): 114530, https://doi.org/10.1016/j.cma.2021.114530.

Appendix A

Computational Procedure for Semi-Implicit ULMPM

The computational flow chart for ULMPM using a semi-implicit scheme is shown in Algorithm 2.

ALGORITHM 2 | ULMPM.

```
if t = 0 then
   Compute particle volume V_p^0, volume fraction θ_αp^0, particle mass m_αp^0
end if
while t ≤ t_end do
   Compute shape function S_Ip and shape function gradient ∇S_Ip
   P2G mapping, m_αI, v_αI
   Compute solid strain and effective stress
   Update particle volume, density, volume fraction, and permeability
   Assemble coefficient matrix in Equations (60), (62), and (66)
   Detect free surface nodes and apply BCs
   Compute intermediate accelerations, a*_αI
   Compute pore pressure increment, Δp_I^{t+1}
   Compute update accelerations, a**_αI
   Update particle velocity v_αp, position x_p, and pressure p_p
   t = t + Δt
end while
```

Appendix B

Pore Pressure Stabilization

To investigate the sensitivity of the stabilization coefficient τ used in the PPP stabilization method (4.3), we perform additional slumping tests with varying τ. Figure B1 presents contours of the pore pressure at the final stage ($t = 0.5$ s) for different stabilization parameters. It is observed that without stabilization ($\tau = 0$), pore pressure fluctuations occur, particularly on the right side of the slumping block. As the value of τ increases, these fluctuations are progressively diminished. And the case with $\tau = 1$ yields a smooth, stable, and physically reasonable pore pressure distribution, indicating that selecting $\tau = 1$ could effectively mitigate numerical instabilities without adversely affecting the physical accuracy of the results.

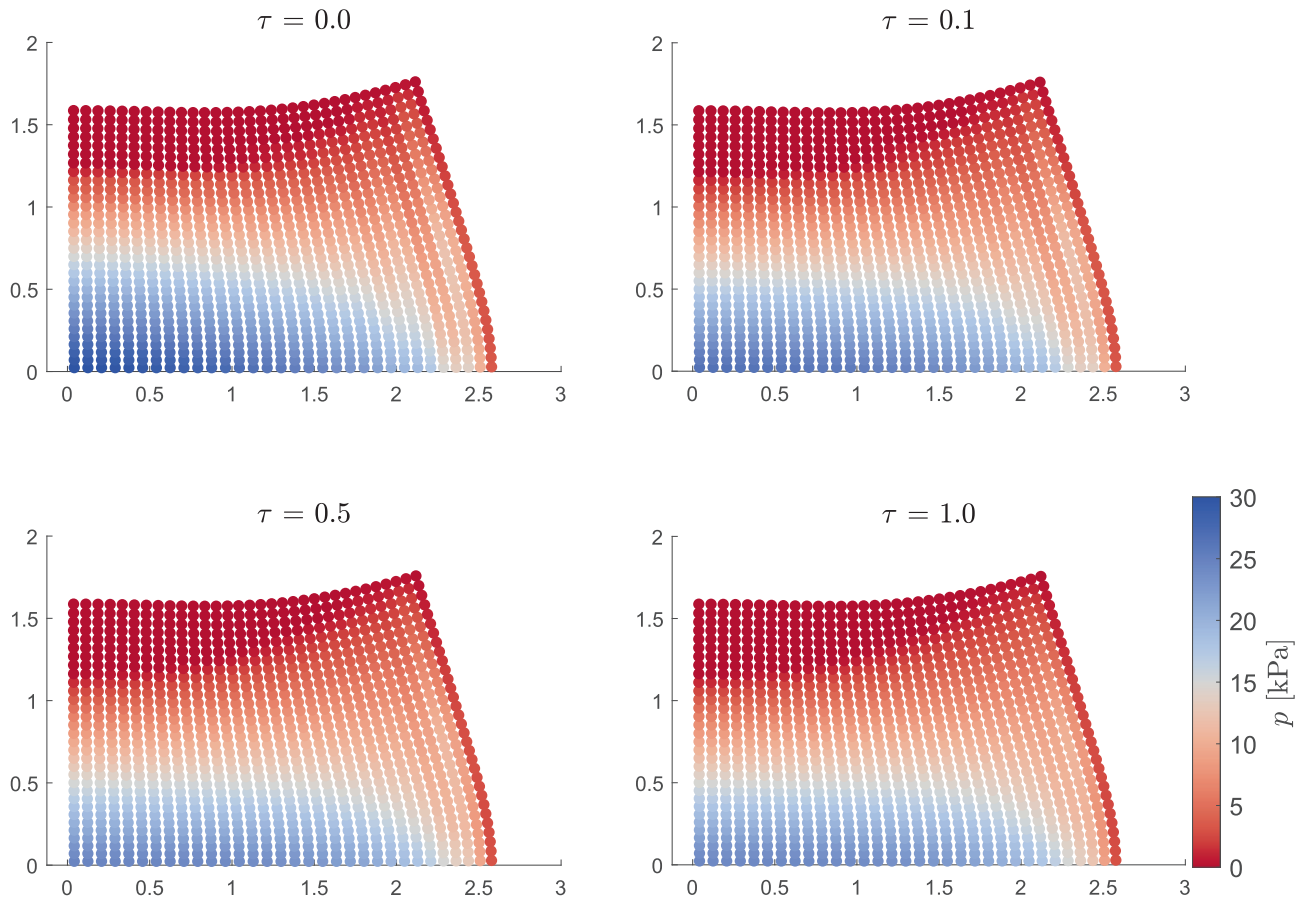

FIGURE B1 | Contours of pore pressure for varying stabilization parameter τ at $t = 0.5$ s.